PHYSICAL REVIEW A VOLUME 50, NUMBER 2 AUGUST 1994

Experimental and theoretical investigation of neonlike selenium x-ray laser spectral linewidths and their variation with amplification

Jeffrey A. Koch,[1] Brian J. MacGowan,[1] Luiz B. Da Silva,[1] Dennis L. Matthews,[1] James H. Underwood,[2]
Philip J. Batson,[2] Richard W. Lee,[1] Richard A. London,[1] and Stan Mrowka[1]
[1]*Lawrence Livermore National Laboratory, P.O. Box 808, L-059, Livermore, California 94550*
[2]*Lawrence Berkeley Laboratory, 1 Cyclotron Road, Berkeley, California 94720*

(Received 16 February 1994)

This paper describes our recent x-ray laser spectral linewidth measurements and discusses the consequences of these measurements. The experiments observed the 206.38- and 182.45-Å laser transitions in neonlike selenium using an extremely high-resolution soft-x-ray spectrometer, and measured the spectral linewidths and relative spectral intensities of the laser lines from amplifiers of varying lengths. The data allow the intrinsic (unamplified) linewidths of the 206- and 182-Å lasers to be extrapolated as 50 and 35 mÅ, respectively. The intrinsic spectral width of the 206-Å laser is somewhat greater than the predicted 43-mÅ Voigt-profile width based on calculated transition rates and on the expected ion temperature in the plasma, and while the number of data points obtained with the 182-Å laser is small and a conclusive comparison with calculations is not possible, the extrapolated intrinsic linewidth of this laser is clearly consistent with the predicted 37-mÅ Voigt-profile width and is not significantly broader or narrower than expected. The data also show significant gain narrowing of both lines with increasing amplifier length and show no significant rebroadening of the 206-Å laser in long, saturated amplifiers. We discuss line broadening and line transfer calculations we have performed which show that the saturated 206-Å laser line transfer behavior can be treated homogeneously due to non-negligible homogeneous lifetime broadening contributions, which significantly reduce inhomogeneous Doppler saturation rebroadening, and due to collisional redistribution rates which are large enough in any case to homogenize the otherwise inhomogeneous Doppler contributions. We also discuss the implications of these results with regard to earlier suggestions that Dicke narrowing effects could play a significant role in determining the intrinsic line profiles of these laser transitions, and we conclude that Dicke narrowing effects are not likely to be significant for either laser.

PACS number(s): 42.55.Vc, 32.70.Jz, 07.85.+n, 52.70.−m

I. INTRODUCTION

The field of x-ray laser research has been characterized by rapid progress since the first successful proof of principle demonstrations [1–3]. Collisional excitation amplified spontaneous emission (ASE) x-ray lasers, which rely on collisional excitation of highly stripped ions in high-temperature laser-produced plasma to produce population inversions in outer-shell $\Delta n = 0$ transitions, have generated much interest due to their brightness and wavelength versatility [4]. Neonlike collisional excitation laser, which are isoelectronic to Ne I and lase on $3p$-$3s$ transitions, have been produced worldwide in many elements with wavelengths as short as 80 Å [5–7]. The analogous nickel-like collisional excitation lasers, lasing on $4d$-$4p$ transitions, have also been produced in a number of elements with wavelengths as short as 36 Å [8]. Preliminary holography experiments have been performed [9] with Ne-like Se, and 500-Å-resolution light-field microscopy with Ni-like Ta [10] has been demonstrated [11] and applied [12] to the imaging of gold-labeled and unlabeled biological specimens. The spatial coherence of the 206.38-Å laser in Ne-like Se has been characterized [13], the saturated energy output of the Ne-like Y laser has been measured [14], and experiments which multipass the laser emission through the gain region have been performed [15,16] with Ne-like Se and Ne-like Ge using normal-incidence multilayer mirrors [17]. More recently, x-ray lasers have been used to investigate hyperfine soft-x-ray line splitting in niobium [18] and have been used as soft-x-ray backlighters to measure plasma density gradients through moiré deflectometry [19]. Numerous potential applications of x-ray lasers are discussed by Elton [4] and in Ref. [20]; reviews of the field through 1991 can be found in Refs. [21] and [22], and details of the basic operation of laboratory x-ray lasers can be found in Ref. [23] and in references therein, as well as in Elton's work [4].

In spite of this rapid progress, a number of basic physics issues in x-ray lasers remain poorly understood. The relatively small amplification of the 182.45-Å $(2p^5_{1/2}3p_{1/2})_{J=0}-(2p^5_{1/2}3s_{1/2})_{J=1}$ line in Ne-like lasers (the "$J=0-1$ anomaly") has never been conclusively explained, though calculations predict it to have large gain [1,2,24]. Lasing in F-like analogs to Ne-like lasers, while predicted [25], has never been observed, in contrast to the observation of lasing in Co-like analogs to Ni-like lasers [26]. The effects of driver beam nonuniformities and plasma turbulence are poorly understood and potentially important [27], and it has only recently become possible to measure x-ray laser linewidths [28,29], in spite of their fundamental importance to gain and radiative transport

1050-2947/94/50(2)/1877(22)/$06.00

calculations, due to the difficulty in obtaining soft-x-ray spectra with sufficient resolution. Ne-like Se x-ray laser linewidths have generally been assumed [1] to be dominated by Doppler broadening, based on a predicted [1,2] ion temperature of 400 eV.

The intrinsic (unamplified) spectral profile of a plasma line is determined predominantly by spontaneous emission rates, electron collisional rates, Stark broadening, and Doppler broadening [30], with possible complications due to ion turbulence [30,31] and additional ion-ion interactions [31,32]. The observed profile is also modified by radiative transport effects. Amplified lines narrow approximately as the square root of the gain-length product in the small signal regime [33]. As the laser saturates, the line can rebroaden to its intrinsic width if the intrinsic profile is dominated by inhomogeneous (i.e., caused by local inhomogeneities such as Doppler shifts, quasistatic electric fields, or turbulence) rather than homogeneous (i.e., Fourier transform limited by fast collisions, spontaneous emission, etc.) broadening mechanisms [34–36]. Measurements of the linewidth of a laser and its variation with amplification thus provide important information on the nature of the broadening mechanisms present and therefore on the local environment in the laser medium. There have been few reported experiments which have measured the amplifier length dependence of ASE (mirrorless) laser linewidths through saturation, and these have generally used the high-gain 3.51-μm xenon laser transition [35,37,38]. Previous measurements of the spectral widths of x-ray laser lines [39–41] did not observe variations with amplifier gain-length product, primarily because instrument resolutions were insufficient.

In this paper we discuss in more detail our recent successful measurements [28,29,42] of the 206.38-Å $(2p^5_{3/2}3p_{3/2})_{J=2}-(2p^5_{3/2}3s_{1/2})_{J=1}$ Ne-like Se x-ray laser linewidths, and we discuss additional measurements we have made on the linewidth of the 182.45-Å $(2p^5_{1/2}3p_{1/2})_{J=0}-(2p^5_{1/2}3s_{1/2})_{J=1}$ Se laser. We also present laser line-broadening and line-transfer calculations which suggest that the line profiles of both lasers can be approximated reasonably well by Voigt profiles with Gaussian and Lorentzian components due to thermal Doppler broadening and lifetime broadening, respectively. We find that the laser line transfer behavior can be treated homogeneously due to non-negligible homogeneous lifetime broadening contributions and due to collisional redistribution rates large enough to homogenize the otherwise inhomogeneous Doppler contribution. We also discuss the implications of these results with regard to the suggestion [31] that Dicke narrowing could be significant for these laser transitions and with regard to more recent calculations suggesting that this may not be the case [43], and we conclude that the experimental data support these calculations.

This paper is organized as follows. Section II describes in detail the spectrometer and detectors used in the experiments. Section III describes the details of the x-ray laser experiments themselves. Section IV discusses how the results were analyzed and presents the reduced experimental data. Section V reviews the line-broadening mechanisms relevant to the selenium x-ray laser. Section VI reviews the laser line-transfer theory relevant to the selenium laser and describes the computer modeling we performed to simulate and compare to the experimental data. Finally, Sec. VII discusses the interpretations of the results and summarizes the conclusions of this research.

II. EXPERIMENTAL INSTRUMENTATION

The high-resolution spectrometer used in this research [44] is unique, though similar in concept to instruments commercially available from Hettrick Scientific, Inc., Richmond, California [45]. It consists essentially of an entrance slit, a concave spherical grazing-incidence mirror, a flat varied-line-space grating [46,47], and a detector placed in an erect focal plane; additional grazing-incidence collecting optics in front of the entrance slit serve to maximize image-plane intensity and to provide spatial resolution of the source. Schematics of the instrument are shown in Figs. 1 and 2, and the relevant specifications are detailed in Table I.

The Au-surfaced spherical mirror $M3$ (20 m radius, 18° included angle) images the entrances slit meridionally to a plane beyond the grating, and the grating intercepts the converging beam and refocuses it onto the detector surface. Wavelength selection is made by rotating the grating about its central groove, maintaining a constant included angle of 18° with the grating operating in the high-dispersion (inner) diffraction orders. The groove separation varies across the grating surface by approximately $\pm 2\%$ from a central value of 1800 lines/mm; the linear variation (≈ 1.2 lines/mm^2) is chosen to provide a nearly erect and stationary image surface so that a flat detector can be mounted perpendicular to the central axis at a fixed distance from the grating, and higher-order variations serve to correct for aberrations. The grating is

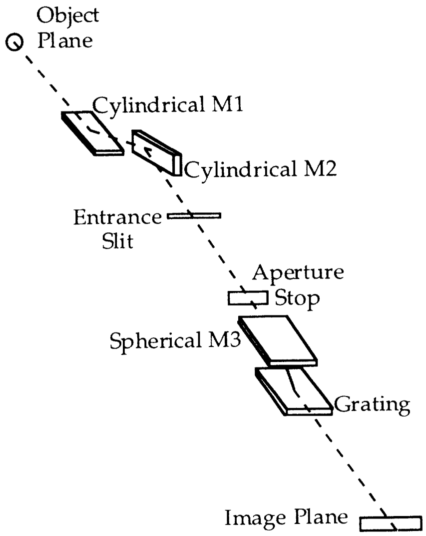

FIG. 1. Schematic of the high-resolution spectrometer used in this research. The source is imaged sagitally onto the focal plane with a magnification of 3 and is imaged meridionally onto the focal plane with a (wavelength-dependent) magnification of approximately 2.8 at 206.38 Å.

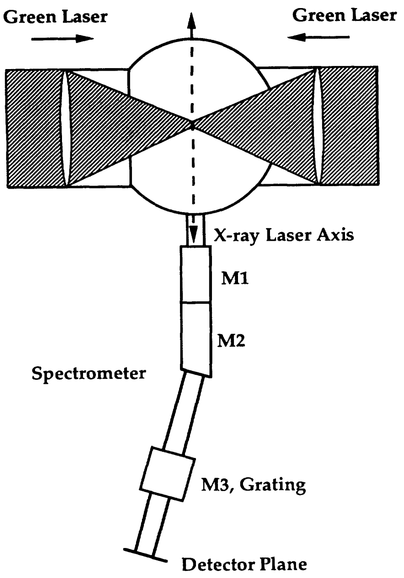

FIG. 2. Sketch of the spectrometer installed at the Nova Laser Facility at LLNL. The total distance between the target chamber wall and the detector is approximately 7.5 m.

a master grating and was mechanically ruled by Perkin-Elmer; it has Au-Pt surface.

The image surfaces for various grating rotation angles, assuming an 18° included angle for $M3$, are shown in Fig. 3. The image surfaces are nearly planar and erect, and

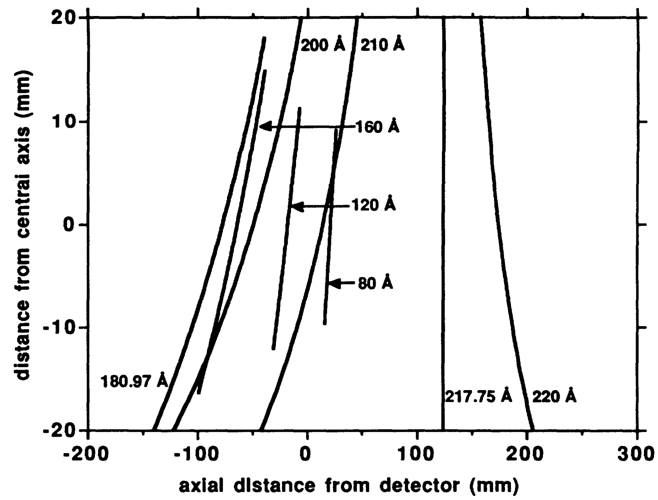

FIG. 3. Side views of the spectrometer focal surfaces for various values of the centered wavelength (along $y=0$, varied by rotating the grating about its central groove). Increasing wavelength is down along each curve, and the lengths of the shorter curves correspond to a ±2 Å range about the central wavelength; their length increases with increasing central wavelength because the dispersion increases (the longer curves are cut off in this graph). The focal surface moves toward the grating as the central wavelength increases to 181 Å, then moves away, becoming erect and planar at approximately 218 Å and moving rapidly towards infinity thereafter.

TABLE I. Relevant dimensions and parameters of the high-resolution spectrometer used in this research.

Quantity	Value	Comments
Distance between chamber center and center of $M1$	1682.7 mm	distances are along the central ray
Distance between center of $M1$ and center of $M2$	457.2 mm	
Distance between center of $M2$ and entrance slit	244.8 mm	
Distance between entrance slit and aperture stop	3023.3 mm	
Distance between aperture stop and center of $M3$	105.5 mm	
Distance between center of $M3$ and center of grating	170.0 mm	
Distance between center of grating and detector plane	2893.3 mm	
ruled grating length	63 mm	master grating, Au-Pt surface
ruled grating width	30 mm	
Collecting-optic length ($M1$,$M2$)	250 mm	flat (bendable) float glass, Rh surface
Collecting-optic width ($M1$,$M2$)	80 mm	
$M3$ length	127 mm	20 m spherical radius, Au surface
$M3$ width	30 mm	
Included angle for grating and $M3$	18°	
Included angle for $M1$ and $M2$	12°	
Grating blaze angle	4.75°	measured from surface plane
Central grating groove spacing	1800 lines/mm	$\sim\pm2\%$ variation along surface

the image distance (from the grating, relative to the fixed detector position) does not change significantly for wavelengths below ~220 Å. However, for wavelengths longer than approximately 180 Å the image distance increases, and the increase becomes rapid above approximately 215 Å, limiting the useful maximum observable wavelength to ~220 Å due to defocusing. The lower wavelength limit of the spectrometer is determined by reflectivity losses from the four optics and is approximately 80–100 Å. The useful range of the instrument is therefore approximately 100–220 Å, a range which covers most of the existing Ne-like x-ray laser wavelengths [4,48]; the range could be extended to somewhat longer wavelengths by varying the included angle of $M3$ or by moving the detector farther away from the grating.

The resolution ($\lambda/\Delta\lambda$) of the spectrometer has been measured to be as high as 35 000 [44] at 160 Å with a 10-μm entrance slit using a Penning soft-x-ray calibration source [49] and Kodak 101 film as the detector medium. We have measured comparable resolutions (25 000–30 000) using the same calibration source and a thinned, backilluminated x-ray charge coupled device (CCD) detector [50] (described below); however, spectral resolutions obtained for the Se x-ray laser experiments were generally lower because larger entrance slit widths were used. The plate scale of the spectrometer varies with wavelength and is approximately 0.100 Å/mm at 182.45 Å and 0.073 Å/mm at 206.38 Å; with a 32-mm-long streak camera cathode slit, the spectrometer provides a wavelength coverage of 2.3 Å near 206 Å and 3.2 Å near 182 Å. The coverage is substantially less with the CCD detector due to the small (~13 mm) active area of the CCD chip.

The two collecting optics are flat, Rh-surfaced float-glass mirrors and are oriented in a Kirkpatrick-Baez configuration [51] (Fig. 1); the included angle of each mirror is 12°. Each collecting mirror is mounted in a bending apparatus which allows the surface figure to be varied in a controlled manner [52,53]. The first (meridional) collecting mirror ($M1$ in Fig. 1) focuses the source onto the entrance slit with a magnification of approximately 0.4, while the second (sagittal) collecting mirror ($M2$ in Fig. 1) focuses the source onto the detector plane with a magnification of approximately 3.0. The grating and the spherical mirror $M3$ then focus the entrance slit meridionally onto the detector plane with a magnification of approximately $\sin\alpha/\sin\beta$, α and β being the incident and diffracted angles measured from the grating plane, respectively, with $\alpha+\beta=18°$. The net meridional source magnification at the detector is thus approximately 2.8 at 206.38 Å and 2.0 at 182.45 Å, comparable to the sagittal source magnification of 3.0. The meridional field of view is limited by the entrance slit width, however (a 10-μm slit provides a 25-μm field at the source), so that generally the spectrometer is operated with slit-limited spectral resolution and one-dimensional spatial resolution along the sagittal (horizontal) axis, with the source spatially integrated meridionally over a width dependent on the entrance slit width and typically 25–50 μm. The length of $M2$ limits the sagittal acceptance angle to ~12 mrad, while the aperture stop limits the meridional acceptance angle to a maximum of 3 mrad; the aperture stop is generally closed to a 0.5-mrad acceptance for maximum spectral resolution.

In order to align and focus the instrument for target-physics experiments, bright white light is shone through a 100-μm-diam optical fiber placed in the target chamber at the desired position (chamber center, defined by television camera reticules to within an estimated 50-μm reproducibility), and the surface figures and orientations of $M1$ and $M2$ are varied until the source is focused optimally onto the entrance slit and onto the detector plane using a 10-μm entrance slit. The spectral resolution can then be optimized and measured with the Penning calibration source, which is mounted above and in front of $M1$ and is viewed by inserting a 45° multilayer mirror into the line of sight between chamber center and the center of $M1$.

Spectral resolution optimization is accomplished in two ways. First, the angle the entrance slit makes with respect to the grating plane is adjustable and is varied until the detector plane spectrum is sharpest, as viewed on an x-ray CCD or a microchannel plate (MCP) intensifier [54]. Second, the incident angle of the central ray on $M3$ is varied by rotating $M3$ about its short axis, with the grating being rotated about its central groove to compensate; this effectively varies the image distance until the focal plane is at the detector. The spectral resolution can then be measured directly with the x-ray CCD (23-μm pixels) or with the MCP intensifier, using a tilted slit in the image plane to expand the spectrum until the spatial resolution limitations of the MCP intensifier (≈ 100 μm) can be neglected (this technique is described in Ref. [55]). We note that long exposures onto soft-x-ray film, done in initial tests at Lawrence Berkeley Laboratory [44], were found to be impractical at the Nova Laser Facility at Lawrence Livermore National Laboratory (LLNL) and were not pursued.

Most of the x-ray laser experiments performed in this research (and all those which observed the 206-Å laser transition) used an x-ray streak camera [56] in the detector plane, and this was a Kentech Instruments, Ltd., low-magnification model backed by an ITT F-4113 image intensifier. The transmission cathode material was 750-Å CsI on 250-Å Al and 1000-Å plastic and was made by Luxel Corporation; the cathode slit was oriented along the dispersion axis of the spectrometer and was 1 mm wide, thus providing time-resolved spectra spatially integrated over an approximately 300 μm horizontal by 50 μm vertical region at the target. The streaked spectra were recorded on Kodak TMX-3200 film placed against the back of the intensifier screen.

The spatial resolution of the streak camera was measured using broad-band x rays transmitted through aluminized Mylar filter sheets and through a (30–35)-μm-wide slit oriented along the sweep axis (perpendicular to the cathode slit axis). The resulting profiles were approximately 80 μm wide [full width at half maximum (FWHM)] on film; accounting for the measured electron optics magnification of 1.2 and for the nonzero slit width, this implies that the camera spatial resolution is ~65 μm (FWHM of the line-spread function) at the cathode plane, corresponding to a 110-μm resolvable period at the 30% modulation transfer function (MTF) level. A measured line-spread function from the streak camera is shown in Fig. 4, along with the corresponding MTF curve.

Two of the experiments performed in this research used a Princeton Instruments, Inc., x-ray CCD based on a thinned, backilluminated, 576×384 EEV chip with 23-μm pixels. This camera provides high sensitivity, dynamic range and spatial resolution, and was used on two experiments observing the 182-Å laser transition. The use of this camera greatly simplified the experiments and the data analysis because alignment difficulties with the streak camera cathode slit were removed, because the time-integrating CCD camera does not require a precisely timed electrical trigger pulse (necessary for streak camera measurements) and because the same camera can be used to measure the spectrometer resolution with the Penning calibration source (the streak camera is not sensitive enough for this). The drawback is that the data are time integrated; however, as will be discussed in Sec. IV, no significant temporal variation was observed in the measured spectral linewidths, so that in practice the only loss of information is the time-resolved peak intensity data obtainable with a streak camera. This drawback is offset somewhat by the sagittal spatial resolution of the target which is afforded with the CCD detector and which is lost with the x-ray streak camera in favor of temporal resolution.

Resolution measurements made during the course of the 206-Å laser experiment series using the Penning calibration source and a tilted slit in the detector plane [55] yielded spectrometer resolutions of 18 250 for most experiments (including the experiment in which the 182-Å laser was observed with a streak camera detector) and 14 000 for the experiments using the shortest two Se targets which observed the 206-Å laser; the resolution profiles were symmetrical and well described by Gaussian functions. Convolution of the measured spectrometer resolution function with the measured streak camera spatial resolution function then yielded total instrument resolutions of 17 000 and 14 000, respectively. The 182-Å laser experiments using a CCD detector were performed later; direct spectral resolution measurements with the Penning calibration source yielded total instrument resolutions of 20 250 for those experiments.

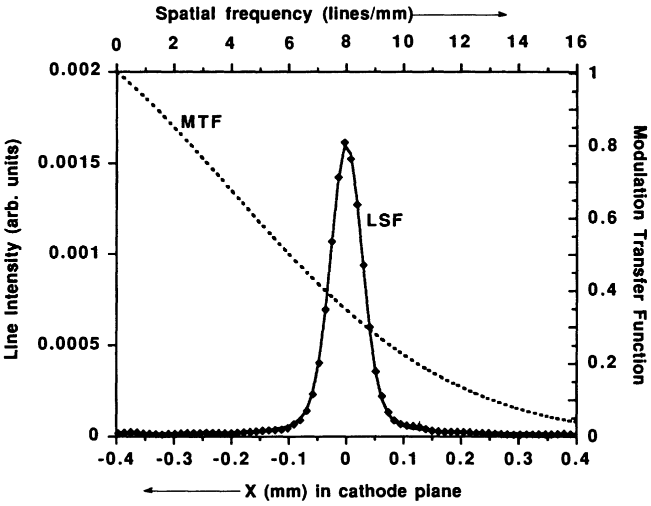

FIG. 4. Plots of the measured streak camera line-spread function (LSF) (bottom and left axes) and the corresponding modulation transfer function (top and right axes). Distances and frequencies are in the cathode plane; images in the film plane are magnified by a factor of 1.2. The solid line is a fit of the data to a Voigt function convoluted with a square function having a width equal to the slit width used (35 μm); the FWHM of the Voigt function is approximately 65 μm. The MTF was calculated from the Fourier transform of the Voigt function alone and falls to 30% at approximately 9 lines/mm, corresponding to a 110-μm period in the cathode plane.

III. Se LASER LINEWIDTH EXPERIMENTS

The x-ray laser experiments were performed in the two-beam chamber of the Nova Laser Facility at LLNL [57]. In these experiments, a selenium exploding foil x-ray laser plasma [1,2] was produced by irradiation of a thin Se/Lexan foil with two $\lambda=0.527$-μm (green) superimposed line-focused beams of the Nova laser. The resulting cylindrical expanding plasma maintains a population inversion between various $3p$-$3s$ levels of the Ne-like charge state of selenium near the axis of the cylinder, where electron temperatures are ≈ 900 eV and electron densities are $\approx 4\times10^{20}$ cm^3 during the ~ 0.5-ns period of optical laser irradiation [1,2,58]. The ASE x-ray laser beam then propagates along the line focus axis in both directions. The laser beam is polychromatic and consists of several laser transitions with varying gains; however, the large dispersion of the spectrometer allowed only one laser transition to be observed on each experiment. Figure 2 shows a diagram of the experimental geometry, and a sketch of the plasma as viewed by the spectrometer is shown in Fig. 5. A more detailed discussion of the 206-Å laser experiments and of the alignment procedures followed is given in Ref. [42].

The foils were nominally ~ 800 Å of Se coated onto one side of ~ 1000 Å of Lexan ($C_{16}H_{14}O_3$), had areal densities of 30–35 μg/cm^2, and were made by Luxel Corporation. The lengths of the foil targets varied between

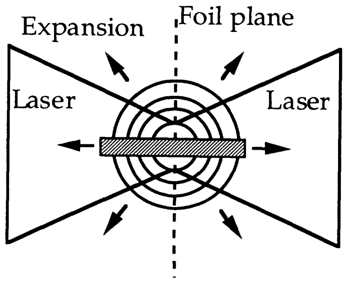

FIG. 5. Sketch of the x-ray laser plasma as viewed from the spectrometer. The laser beams are incident from the right and left onto the target foil (dotted line, viewed edge on), producing a rapidly expanding cylindrical plasma (arrows). The spectrometer views a strip of this plasma (shaded box) approximately 40–60 μm wide (up and down) and 300 μm long (left and right).

0.42 and 6.3 cm. In the experiments, each foil target was placed at the center of the two-beam chamber and aligned so that the plane of the foil bisected the sagittal angular acceptance of the spectrometer; the data were thus angularly integrated over a ± 6-mrad sagittal region (perpendicular to the foil plane) and angularly integrated over a ($\pm 0.25-\pm 1.5$)-mrad meridional region (in the foil plane) depending on the aperture stop width used in the particular experiment. The spectrometer was operated with a narrow entrance slit (typically 15–25 μm), so that the resulting data were spatially integrated over an approximately (40–60)-μm-wide region in the foil plane (see Fig. 5). When a streak camera detector was used, the data were also spatially integrated over a ~ 300-μm-long region perpendicular to the foil plane due to the 1-mm-wide streak camera cathode slit; when a CCD detector was used, the time-integrated data were spatially resolved perpendicular to the foil plane.

The two line-focused beams of Nova were superimposed to an estimated 50-μm reproducibility and collinear to an estimated 1-mrad accuracy. The line focus length of each beam is adjustable by means of two negative cylindrical lenses in front of a $f/4.3$ spherical focusing lens, and their orientation can be varied to produce line foci lengths between ~ 0.5 and ~ 5 cm; a third cylinder lens can be installed to produce line foci up to 7.5 cm long. On each experiment, the foil targets were overfilled by the laser beams along their length in order to minimize bulk axial velocity gradients caused by irradiance variations [23]. The average irradiance on each target was maintained at $(6.0-8.0)\times 10^{13}$ W/cm^2 by varying the Nova beam energy for foil targets of different lengths. In all experiments, the beam focus was ~ 150 μm wide and the laser pulse was 600-ps duration (FWHM) in an approximately Gaussian temporal shape.

The targets used for the 206-Å laser experiments had lengths of 0.42, 0.94, 1.68, 2.55, 3.35, 5.04, and 6.30 cm; two experiments were performed with 6.30-cm targets and the other lengths were shot once each. The targets used for the 182-Å laser experiments had lengths of 0.84, 1.68, and 4.2 cm; each length was shot once, with the first two experiments using a CCD detector and the last using the same x-ray streak camera used in the 206-Å laser experiments. The x-ray laser output intensity varies by several orders of magnitude over this amplifier length range, so that filtering was required with most targets in order to avoid saturating the detector. This was accomplished with thin (2000-Å–4-μm), free-standing aluminum filters placed between the spherical mirror $M3$ and the entrance slit. Filter transmissions were calibrated at the U.S. National Institute of Standards and Technology for wavelengths between ~ 170 and 210 Å.

An example of the resulting streak camera data is shown in Fig. 6. In that experiment, the spectrometer monitored the 206-Å laser transition from a 6.3-cm target, using a ~ 15-μm entrance slit width, a ~ 0.5-mrad tangential acceptance angle, and 3.73 μm of Al filtering. An example of the CCD data from the 182-Å laser experiments is shown in Fig. 7. In that experiment, a 1.68-cm target was observed, using a ~ 15-μm entrance slit width, a 1.25-mrad tangential acceptance angle, and no filtering. The double line to the short-wavelength side of the Se laser is the H-like carbon $3d$-$2p-3p$-$2s$ transition originating from the Lexan side of the target foil. The carbon expands outwards in time, producing a broad emission region in this time-integrated and spatially resolved data; the contrast between the two peaks improves farther out in space because the densities are less there, resulting in less Stark broadening and a narrower spectrum. Finally, the known wavelength of this carbon transition and the high resolution of this spectrum allows the wavelength of the selenium laser to be calibrated at 182.45 Å, consistent with previous calibrations (see, for example, Ref. [48] and references therein).

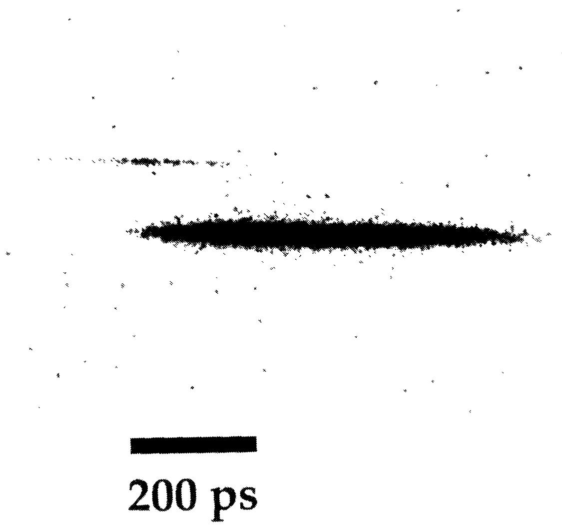

FIG. 6. 206.38-Å laser data from one of the 6.3-cm targets, obtained with an x-ray streak camera. Time is to the right and wavelength is down. The narrow streak at the upper left is a time fiducial (described in Ref. [86]).

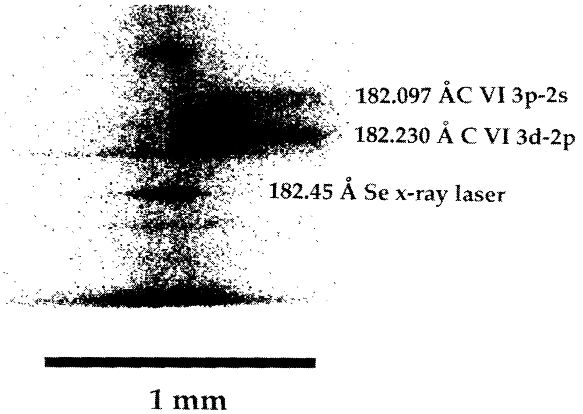

FIG. 7. 182.45-Å laser data from a 1.68-cm target, obtained with an x-ray CCD detector. Wavelength is down and space is to the right and left; the data are time integrated. The doublet above the Se laser is the H-like carbon Balmer α, originating from the Lexan side of the foil target; the other lines have not been identified. The contrast between the $3d$-$2p$ and $3p$-$2s$ peaks improves farther out in space because the densities are lower there, resulting in reduced Stark broadening.

IV. EXPERIMENTAL RESULTS

Relative peak intensity values for each 206-Å laser experiment were measured along with the linewidths and were obtained through film densitometry. The instrument is not absolutely calibrated, so absolute intensity measurements were not obtained; however, estimated absolute units can be obtained by comparison of the present relative intensity data with previous absolutely calibrated intensity data [23], as will be discussed below. The relative intensities were calculated using known streak camera sweep speed, spectrometer dispersion, spectrometer slit setting, and filter transmission corrections; these and other corrections are discussed in more detail in Ref. [42]. Absolute sensitivity comparisons between the streak camera and the CCD detector were not obtained, so that only the two 182-Å laser experiments using the CCD detector can be meaningfully compared in relative intensity; however, previous data on the target-length scaling of the intensity of this laser have been published [23].

Peak intensities were measured at the temporal peak of the time-resolved emission data, which generally showed temporal widths on the order of 250 ps (FWHM); the longer targets showed somewhat longer emission durations than the shorter ones, likely due to speed-of-light transit-time effects in the amplifiers. The relative peak intensity data were then corrected for instrument broadening, which slightly reduces the measured peak intensities as well as broadens the measured linewidths [the corrected relative peak intensity is approximately equal to the measured peak intensity times the ratio of the measured linewidth to the reduced (deconvolved) linewidth]. This small correction affects the longer target data somewhat more than the short-target data, simply because the instrument resolution becomes more significant as the laser linewidth narrows.

Several additional small (but systematic) experimental effects were present in the intensity data and were removed for quantitative analysis. The most significant of these are the effects of spatial integration over a spatially varying laser emission region and the effects of bulk Doppler detuning of the edges of the foil amplifier. In addition, approximate absolute spectral intensity units can be applied to the peak intensity data by careful comparisons with previous spectrally integrated, absolutely calibrated data [23].

The spectrometer spatially integrated the emission of the plasma being viewed over a ~ 50-μm (vertical) by ~300-μm (horizontal) region (see Fig. 5). Because the effective emission region of the Se laser narrows from ~250 to ~50 μm as the target length is increased [59], the measured peak intensities should be divided by the effective source size (within the field of view of the spectrometer) to obtain corrected relative peak intensities, which correspond to the laser spectral intensity along the axis of the amplifier. This correction was also made in the data compilation of MacGowan [23].

The effects of bulk Doppler detuning of the edges of the foil x-ray laser targets can be estimated and removed from the intensity data as well. This occurs because pressure gradients force the exploding foil plasma to expand in all directions; the edges of the foil will therefore expand towards and away from the spectrometer. Expansion velocities are on the order of 10^7 cm/s [60], so that the edges of the foil are effectively Doppler detuned from the rest of the target. Hydrodynamics simulations suggest that the total detuned depth of the plasma is ~0.5 mm, independent of target length, and so the effective amplifier length of each target is simply 0.5 mm less than the actual target length; this small correction clearly affects the shorter targets more than the longer ones.

Next, for comparison with previous experimental intensity data [23], the present spectrally resolved intensities were multiplied by the corresponding reduced spectral linewidths (discussed below) so that the two data sets could be compared directly (it should be noted that both data sets are angularly integrated). This comparison allowed a calibration to be made by superimposing the two data sets in order to estimate absolute spectrally integrated intensity units for the present data (Fig. 8); division of each intensity by the corresponding reduced spectra linewidth then recovered the desired absolutely calibrated peak spectral intensity values.

The resulting peak (in time, spectrum and space in the amplifier) intensity data for the 206-Å laser is shown in Fig. 9. The peak intensity is seen to exponentially increase nearly seven orders of magnitude from 0.42-cm targets to (3–4)-cm targets; this is followed by reduced gain in longer targets due to saturation. The long-amplifier rollover in the gain does not by itself show that the laser is saturated, since the increasing effects of beam refraction and scattering due to density fluctuations in longer amplifiers could yield a similar effect; the data of MacGowan [23] does, however, provide convincing evidence of the saturation of this laser in long (>3 cm)

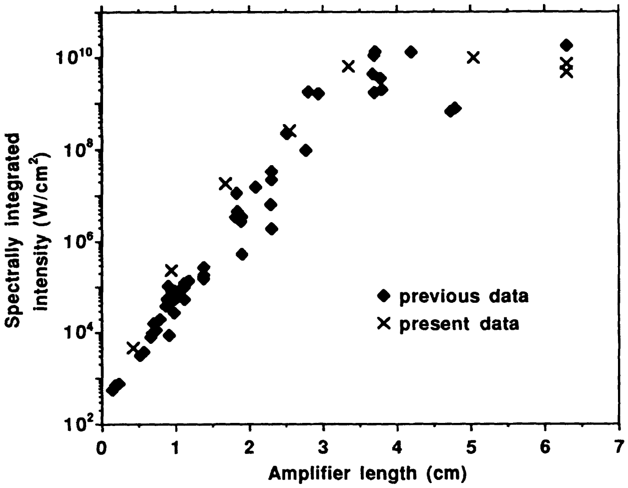

FIG. 8. Compilation of previous spectrally integrated, absolutely calibrated 206-Å laser intensity data from Ref. [23] plotted with the spectrally integrated data from the present experiments. The absolute ordinate units are used to associate an absolute spectrally integrated intensity with each data point in the present experiments, thus allowing the measured peak spectral intensity data to be calibrated.

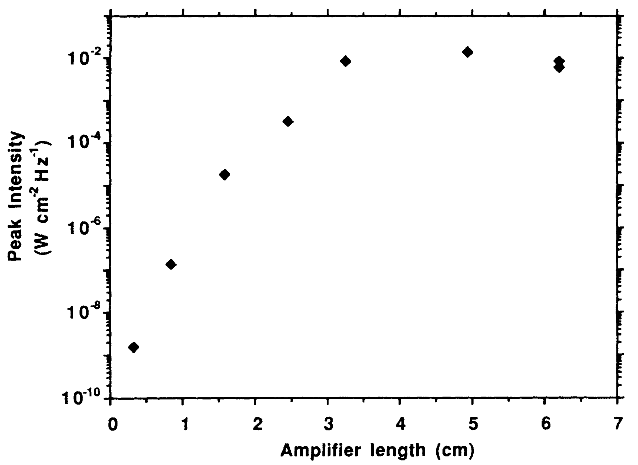

FIG. 9. Peak spectral intensity (in the spectrum, time and space in the amplifier) of the 206-Å laser as a function of amplifier length, corrected as described in the text. The ordinate units are approximate and were obtained by comparison with the absolutely calibrated data of Ref. [23] (Fig. 8).

amplifiers through relative intensity comparisons between laser lines with different gain (discussed further in Ref. [42]). Finally, we note that the two 182-Å laser experiments using a CCD detector (with target lengths of 0.84 and 1.68 cm) showed peak intensities (resolved in space and spectrum but time integrated) which were nearly equal, with the longer target yielding an intensity approximately 50% greater than the shorter target. This observation is inconsistent with previous measurements of the gain coefficient of this laser ($\sim 2\ \mathrm{cm}^{-1}$ [23]), and possibly results from alignment variations; in any case the measured spectral widths were significantly different, as discussed below, and we were unable to further investigate this unusual result with additional Nova experiments.

The measured spectral linewidths also required reduction before quantitative analysis could be made. First, the broadening due to finite instrument resolution had to be removed from the data, using the measured spectrometer resolution and including the measured streak camera spatial resolution function for those experiments using a streak camera detector (the latter consideration does not apply in the experiments using a CCD detector, as the Penning calibration source measurements and the x-ray laser data were all taken with the same detector). The spectrometer resolution for the experiments using a streak camera detector was measured using a tilted-slit technique [55], as discussed above, and the resulting resolution profile was nearly Gaussian over a peak signal-to-noise ratio of approximately 100, so that a Gaussian resolution profile was assumed. The streak camera resolution function was also measured, and the profile was well described by a Voigt function over a peak signal-to-noise ratio of approximately 100; the resulting total instrument resolution was therefore approximately a Voigt function also.

In order to remove the instrument resolution function from the 206-Å laser data (and from the 182-Å laser data obtained with a streak camera detector), the data profiles were fit to various functional forms, including Voigt functions, and the spectrometer and streak camera resolution functions (the latter also fit to several functional forms including a Voigt function) were then deconvolved from the data profiles analytically (this is discussed in detail in Ref. [42]). The value of the resulting reduced spectral linewidth (FWHM) for each experiment depended on how the profiles were fit, and the spread in values thus obtained was taken as a measure of the uncertainty in the deconvolution process for all streak camera detector experiments except the shortest-target 206-Å laser experiment, in which signal-to-noise uncertainties dominated the uncertainty. Finally, the raw data for the 182-Å experiments using a CCD detector was reduced by fitting the instrument resolution profile and the x-ray laser data profiles to Gaussian functions and analytically deconvolving the former from the latter.

The other correction applied to the spectral linewidth data was the approximate removal of bulk Doppler detuning effects from the edges of the foil (described above), which was simply the subtraction of 0.5 mm from the actual target length to obtain an effective amplifier length. The spatial integration correction applied to the intensity data was not applied to the spectral linewidth data because the correction is not straightforward and depends on how the laser saturates, i.e., whether the laser rebroadens upon saturation. This effect was, however, modeled using different line profiles and broadening mechanisms, and we conclude that the effect of spatial integration on the measured spectral linewidths is essentially negligible [42].

The measured and reduced spectral linewidth values (FWHM), together with the estimated error bars, for the 206- and 182-Å lasers are shown in Figs. 10 and 11, respectively. The reduced linewidth values are likely to be somewhat conservative (on the small side) because the measured spectrometer resolution values are naturally lower bounds due to nonzero calibration source linewidths. Similarly, the error bars are likely to be con-

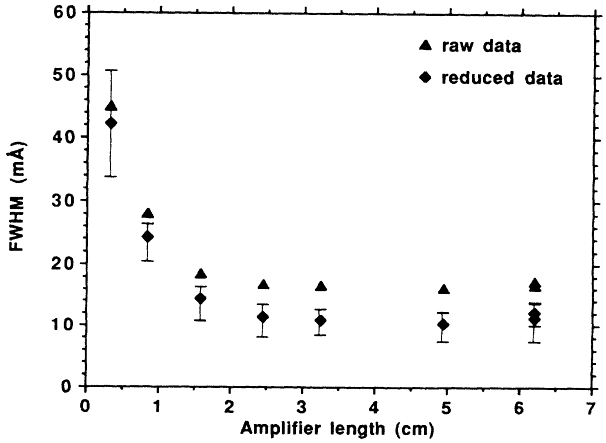

FIG. 10. Measured and reduced spectral linewidths (FWHM) for the 206-Å laser as functions of amplifier length. The error bars for shortest target are due to background level uncertainties; for the others, they represent the spread in reduced widths obtained using different fitting functions.

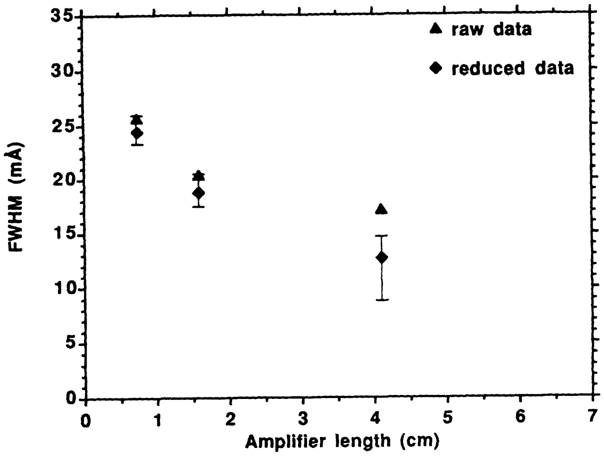

FIG. 11. Measured and reduced spectral linewidths (FWHM) for the 182-Å laser as functions of amplifier length. The error bars for the longest target represents the spread in reduced widths obtained using different fitting functions; for the other experiments (using an x-ray CCD detector), a 10% uncertainty is assumed.

servative (on the large side), especially the lower limits, because the actual spectrometer resolution, the most significant factor in the deconvolution, is somewhat better than the values measured and because the various deconvolution procedures used gave a variety of reduced spectral line shapes, some of which (particularly those with the narrowest widths) had unrealistically large wings in the line profiles. It should be understood that the laser spectral line profiles themselves were not accurately measured due to finite instrumental dynamic range and due to non-negligible instrument broadening which obscures the shape of the profile being measured; the important measurements were of the spectral linewidths.

The 206-Å laser data in Fig. 10 shows significant gain narrowing of the laser line profile with increasing amplifier length out to approximately 2–3 cm; for longer targets, the linewidth remains constant within experimental uncertainty at approximately 10 mÅ, giving a saturated laser bandwidth ($\lambda/\Delta\lambda$) of 20 000. This behavior is consistent with a homogeneously broadened intrinsic line profile [34,36], as will be discussed in more detail in Sec. VII; no spectral saturation rebroadening was observed. The intrinsic linewidth, extrapolated to a target length of zero, is approximately 50±10 mÅ and is clearly significantly larger than the predicted 400-eV ion-temperature Doppler width of 36 mÅ [1,2]. The 182-Å data in Fig. 11 also shows significant gain narrowing with increasing amplifier length and indicates an extrapolated intrinsic linewidth of approximately 35 mÅ; this laser is not saturated in any of these experiments, so that only the small-signal behavior is observed. Finally, we note that no significant time dependence to the measured spectral linewidth was observed in any time-resolved experiments. This is to be expected because the spectral width of a laser line (in the small-signal regime) narrows as the square root of the gain-length product, while the peak intensity grows as the exponential of the gain-length product. The linewidth thus varies slowly with intensity (as the square root of the logarithm of the intensity), so that the finite dynamic range of the instrumentation (≈ 100) precluded the observation of significant temporal variations in the linewidth [42].

The 206-Å data from a complete series of linewidth measurements for an x-ray laser. The data clearly show gain narrowing of the line profile from short and intermediate-length targets in both the raw data and in the reduced data. The intrinsic linewidth (extrapolated to $L=0$) is ~50 mÅ ($\lambda/\Delta\lambda \approx 5000$), significantly larger than the calculated Doppler width of 36 mÅ, and the line profile narrows to 10 mÅ in targets longer than several centimeters. In addition, no significant saturation rebroadening was observed with long, saturated targets; this suggests that the intrinsic line profile is dominated by homogeneous broadening mechanisms (such as electron-collisional broadening, for example) rather than by (generally) inhomogeneous broadening mechanisms such as Doppler broadening; in any case, saturation appears homogeneous. This is interesting because the intrinsic line profiles of these lasers are expected to be dominated by thermal Doppler broadening, so that some saturation rebroadening might be expected. In Sec. VII we will show that this apparent discrepancy can be explained by the strong reduction in inhomogeneous saturation rebroadening due to even relatively small lifetime broadening contributions and by collisional redistribution effects which serve to homogenize the otherwise inhomogeneous Doppler component. It appears unnecessary (and, likely, incorrect, as will be discussed in Sec. V) to invoke additional complications due to Dicke narrowing effects, as was previously suggested [28].

Finally, the 182-Å laser data are roughly consistent with the 206-Å data, showing gain narrowing from a ~35-mÅ intrinsic linewidth ($\lambda/\Delta\lambda \approx 5000$) and narrowing to $\lambda/\Delta\lambda = 14\,000$ in targets with small-signal amplification gain-length products ≈ 10. While the paucity of 182-Å data here precludes a precise intrinsic linewidth extrapolation, it is clear that the extrapolated intrinsic linewidth is not unusually broad or narrow in comparison with the 206-Å laser. The extrapolated width is in fact consistent with Voigt-profile estimates, and this observation supports the conclusion [43] that Dicke narrowing effects are not significant in the Se laser, as will be discussed in Sec. V.

V. LINE BROADENING IN THE Se LASER

This section reviews the line-broadening mechanisms relevant to the selenium laser and estimates their significance on the basis of previously calculated densities, temperatures, collisional rates, etc. Based on those parameters, the dominant contribution to the intrinsic linewidth of both Se lasers is expected to be thermal Doppler broadening, and additional broadening due to spontaneous emission and electron collisions is expected to be relatively small. Dicke narrowing and its relevance are also discussed. We review these issues in some detail here in order to summarize the line-broadening issues relevant to the present experimental measurements and their relationship to laser spectral narrowing and saturation rebroadening.

The Wiener-Khinchine theorem [61,62] states that the (unnormalized) spectral density $S(\omega)$ of a radiating system is related to the autocorrelation function $g(\tau)$ of its radiated electric field $E(t)$ through a Fourier transform

$$S(\omega)=\frac{1}{\pi}\int_0^{\infty}\cos(\omega\tau)g(\tau)d\tau\ , \tag{1}$$

where, for real electric fields,

$$g(\tau)\equiv\langle E(t+\tau)E(t)\rangle \tag{2}$$

and, for complex electric fields,

$$g(\tau)\equiv\mathrm{Re}\langle E^*(t+\tau)E(t)\rangle\ . \tag{3}$$

The angular brackets denote either a time average for a single radiator or an ensemble average for an ensemble of radiators [62], and the asterisk refers to the complex conjugate of the field.

The correlation function tracks the temporal coherence of the field which would be produced by an oscillator or by an ensemble of oscillators which radiate in phase at time t, and incoherence caused by Doppler shifts (due to radiator motion), phase-interrupting collisions common to each radiator, etc. will cause the phase of the field at time $t+\tau$ to become less correlated to the phase of the field at a previous time t. As the correlation function decays in time, the spectrum (the Fourier transform of the correlation function) will broaden in frequency; a broader correlation function (in time) will give rise to a narrower spectrum (in frequency) and vice versa. Temporal incoherence thus relates directly to spectral line broadening.

Homogeneous incoherence essentially results when the field radiated by an oscillator has finite temporal coherence, e.g., when the radiation field has finite duration. Inhomogeneous incoherence results when the individual radiators in an ensemble have different oscillation frequencies ω_0, and the superposition of these frequencies results in the appearance of damping in the ensemble-averaged correlation function. Thus, in a homogeneously broadened ensemble of atoms, the radiated field of each individual atom has the same spectrum, and the spectrum of the ensemble is the same as the spectrum of each individual atom. In an inhomogeneously broadened ensemble of atoms, the spectrum of each atom is different in that each atom radiates at a different frequency, and the spectrum of the ensemble is the superposition of the (different) spectra of the individual atoms. The distinction is important in the present context because inhomogeneously broadened and homogeneously broadened lasers show different saturation behaviors, and in particular inhomogeneous broadening induces rebroadening of the linewidth in saturated amplifiers after initial gain narrowing in the small-signal regime. We discuss the following broadening mechanisms: Doppler broadening, lifetime broadening due to spontaneous emission and fast inelastic collisions, and Dicke narrowing.

Radiator motion generally produces inhomogeneous line broadening by superimposing the radiation frequencies from many atoms, each of which is moving at a somewhat different velocity along a particular line of sight. The frequency ω of the radiation observed from each atom depends on its velocity v through the Doppler shift $\omega=\omega_0(1+v/c)$, so that the superposition of the different frequencies maps out the velocity distribution function along that line of sight. In thermal equilibrium, this distribution function is Maxwellian (Gaussian), so that the usual Doppler-broadened line profile is Gaussian.

Doppler broadening can also be considered within the framework of the field autocorrelation function Eq. (3) discussed above [32,62], and this more rigorous approach is described here because it illustrates the limits of validity of the usual inhomogeneous Doppler-broadening model. The complex electric field emitted from a fixed radiator at position $\mathbf{r}$ and at time t is assumed to have an oscillatory dependence

$$E\propto\exp(i\mathbf{k}_0\cdot\mathbf{r}-i\omega_0 t)\ , \tag{4}$$

where k_0 is the wave-number vector and ω_0 is the oscillation frequency. For a radiator which moves in time, the field at a fixed point in space will vary because $\mathbf{r}$ will itself vary in time, so that the field produced by a moving atom becomes

$$E\propto\exp[i\mathbf{k}_0\cdot\mathbf{r}(t)-i\omega_0 t]\ , \tag{5}$$

where $\mathbf{r}$ is written as the time integral of the velocity vector

$$\mathbf{r}(t)=\mathbf{r}_0+\int_0^t\mathbf{v}(t')dt'\ . \tag{6}$$

The field autocorrelation function Eq. (3) is then

$$g(\tau)=\mathrm{Re}\langle\exp[-ik_0 r(\tau)+i\omega_0\tau]\rangle\ , \tag{7}$$

where

$$\mathbf{r}(\tau)\equiv\int_t^{t+\tau}\mathbf{v}(t')dt' \tag{8}$$

with the angular brackets in Eq. (7) representing an ensemble average. If the oscillators do not ever collide and change their velocities, then $\mathbf{r}(\tau)$ is simply the (fixed) velocity multiplied by τ,

$$\mathbf{r}(\tau)=\mathbf{v}\tau\ . \tag{9}$$

Then, for a (nonrelativistic) Maxwellian velocity distribution within the ensemble

$$f(\mathbf{v})=\left[\frac{m}{2\pi kT}\right]^{3/2}\exp\left[\frac{-m|\mathbf{v}|^2}{2kT}\right]\ , \tag{10}$$

the correlation function Eq. (7) is

$$\begin{aligned}g(\tau)&=\mathrm{Re}\left[\exp(i\omega_0\tau)\int_{-\infty}^{\infty}\exp(-i\mathbf{k}_0\cdot\mathbf{v}\tau)f(\mathbf{v})d\mathbf{v}\right]\\&=\exp\left[\frac{-k_0^2\tau^2}{4\left[\dfrac{m}{2kT}\right]}\right]\cos\omega_0\tau\ .\end{aligned} \tag{11}$$

A Fourier transform then yields the usual area-normalized Doppler line profile [63]

$$L(\omega)=\frac{c}{\omega_0}\left[\frac{m}{2\pi kT}\right]^{1/2}\exp\left[\frac{-mc^2(\omega-\omega_0)^2}{2kT\omega_0^2}\right] . \tag{12}$$

The collision-free formalism can still be applied if the velocities change over time scales long compared with the effective radiative lifetime of the oscillator (i.e., the inverse of the homogeneous spectral linewidth, discussed below); in some circumstances, however, the breakdown of this approximation can have significant consequences which are of interest here. One is the effective "homogenization" of the ordinarily inhomogeneous Doppler profile when the mean velocity-changing collision interval t_c is less than the effective radiative lifetime (collisional redistribution or cross relaxation [64]); another is collisional narrowing of the Doppler profile when t_c is shorter than the effective Doppler correlation time (Dicke narrowing [65]).

The exponential in Eq. (12) can be written in terms of the frequency full width at half maximum

$$\exp\left[\frac{-mc^2(\omega-\omega_0)^2}{2kT\omega_0^2}\right]=\exp\left[\frac{-4\ln2(\omega-\omega_0)^2}{(\Delta\omega)^2}\right] , \tag{13}$$

where the FWHM $\Delta\omega$ is equal to

$$\begin{aligned}\Delta\omega&=\omega_0\left[\frac{8kT\ln2}{mc^2}\right]^{1/2}\\&\approx7.7156\times10^{-5}\omega_0\left[\frac{T_i\ (\mathrm{eV})}{m_i(\mathrm{amu})}\right]^{1/2} .\end{aligned} \tag{14}$$

Using a 400-eV ion temperature estimate for the Se x-ray laser plasma [2] and an atomic mass of 78.9 for selenium, the relative Doppler width for the Se laser would be

$$\frac{\Delta\omega}{\omega_0}=\frac{\Delta\lambda}{\lambda_0}=1.74\times10^{-4} . \tag{15}$$

Thus, for the 206-Å laser the expected Doppler width is 36 mÅ and for the 182-Å laser the expected Doppler width is 32 mÅ.

A number of processes can cause homogeneous lifetime broadening of a spectral line. These include radiative decay (spontaneous emission) and electron collision-induced transitions. These processes are homogeneous because they affect each radiator in an ensemble in the same way and can be considered to cause spectral line broadening by limiting the coherent emission duration of each radiator in an ensemble.

Spontaneous emission can be considered to cause the probability of a particular atom being found in excited state j to exponentially decay in time, with a rate A_j given by the sum of the spontaneous transition rates from level j to all lower-energy states [66]; for dipole transitions, these rates are the Einstein A coefficients [67]

$$A_j=\sum_k A_{jk}=\sum_k\frac{4}{3\hbar^4c^3}(E_j-E_k)^3|\langle j|\mathbf{d}|k\rangle|^2 , \tag{16}$$

where (E_j-E_k) is the energy difference between states j and k and the d^2 term is the square of the dipole matrix element connecting states j and k. Since the probability $\langle\Psi_j(t)|\Psi_j(t)\rangle$ decays at a rate A_j, the wave function amplitude evidently decays at a rate of $A_j/2$.

The effects of this decaying probability upon the spectral linewidth can be derived in a number of ways, but can be understood as follows. The radiated field of a dipole oscillator is proportional to its (time-dependent) dipole moment [63], and quantum mechanically the dipole moment of an atom radiating between states j and i is $\langle\Psi_j(t)|\mathbf{d}|\Psi_i(t)\rangle$; if both states j and i can spontaneously decay to other levels, the wave-function amplitudes will decay with rates $A_j/2$ and $A_i/2$, respectively. The radiated field $E(t)$ will therefore be proportional to

$$E(t)\propto\cos(\omega_{ji}t)\exp\left[-\frac{(A_j+A_i)t}{2}\right] , \tag{17}$$

where

$$\omega_{ji}\equiv\frac{(E_j-E_i)}{\hbar} . \tag{18}$$

The radiated field thus decays with a rate given by one-half the sum of the spontaneous emission rates out of both levels involved in the transition; the Fourier transform of the decaying exponential then yields the spectrum, as in Eq. (1),

$$S(\omega)=\int_0^\infty\cos(\omega t)\cos(\omega_{ji}t)\exp\left[-\frac{(A_j+A_i)t}{2}\right]dt . \tag{19}$$

For $(A_j+A_i)\ll\omega_{ji}$, the antiresonant term in the resulting line profile (involving $\omega+\omega_{ji}$) can be neglected [61], yielding a Lorentzian line profile. The usual area-normalized spontaneous emission (natural) [63] line profile is then

$$L(\omega)=\frac{2}{\pi\Delta\omega}\frac{1}{1+\dfrac{4(\omega-\omega_{ji})^2}{(\Delta\omega)^2}} , \tag{20}$$

where

$$\Delta\omega=\sum_k(A_{jk}+A_{ik}) . \tag{21}$$

The spontaneous emission rates connecting the various levels in the Ne-like Se ion have been calculated previously [2], and the most important rates for the 206- and 182-Å lasers are shown in Figs. 12 and 13, respectively. Summing the spontaneous emission rates for both lasers, the natural linewidths are found to be 9 mÅ for the 206-Å laser and 5 mÅ for the 182-Å laser.

Electron collisional excitation and deexcitation cause spectral line broadening in a manner similar to spontaneous emission, i.e., by limiting the effective lifetimes of atomic states. When the effective duration of these inelastic collisions is short compared to time scales relevant to the autocorrelation function Eq. (2), e.g., short compared with spontaneous emission lifetimes, then the time-dependent details of the perturbed atomic wave function during the interaction become unimportant and only net changes in the wave function need to be account-

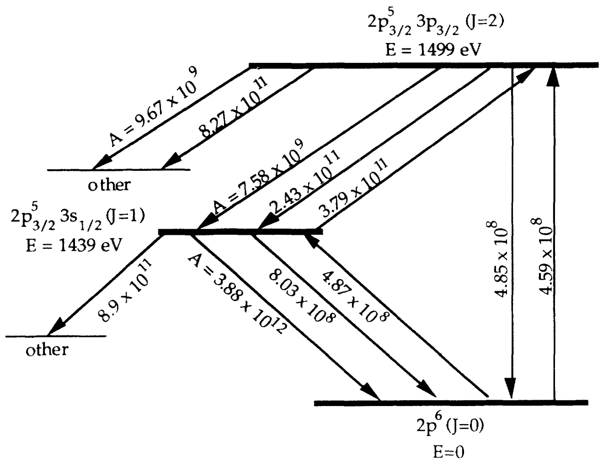

FIG. 12. Level and rate diagram for the 206-Å Se laser, using rates from Ref. [2] and from unpublished LLNL calculations. The spontaneous emission rates are preceded by $A=$ and the collisional rates appear by themselves.

ed for [30]. This is the impact limit of collision broadening, discussed in Ref. [30], and is homogeneous because the collisions affect each atom in the same way and broaden the spectrum of each atom essentially equally. A simple treatment assumes that the radiation of an atom is instantly interrupted by such a collision [63].

The form of the interruption-broadened line profile is the same as that found for spontaneous emission, a Lorentzian with a FWHM $\Delta\omega$ given by the sum of all collisional excitation and deexcitation rates out of the two laser levels [63]. The electron collision broadened width for the Se laser lines can be found by summing the collision rates listed in Figs. 12 and 13, giving Lorentzian linewidths of 5 mÅ for the 206-Å laser and 4 mÅ for the 182-Å laser. It should be understood that the collision rates are time dependent because the densities and temperatures change in the rapidly expanding plasma laser medium; the rates used here (from Ref. [2] and from additional unpublished LASNEX hydrodynamics simulations data, described in Ref. [68]) are the values expected near the temporal peak of the x-ray laser emission, which roughly corresponds to the temporal peak of the optical pump laser [58].

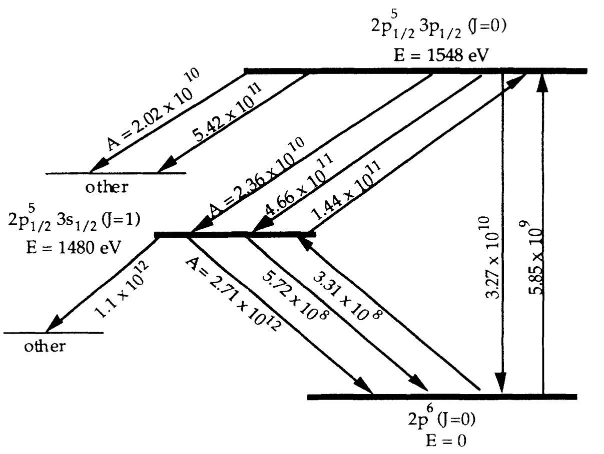

FIG. 13. Level and rate diagram for the 182-Å Se laser, using rates from Ref. [2] and from unpublished LLNL calculations. The spontaneous emission rates are preceded by $A=$ and the collisional rates appear by themselves.

Spontaneous emission and electron collisions can be considered to be statistically independent, so that the correlation function including both effects is found by multiplying the (exponential) correlation functions corresponding to each process. This yields an exponential correlation function with a decay rate equal to the sum of the two individual decay rates, so that the homogeneous lifetime-broadened line profile due to spontaneous emission and electron collisional excitation and deexcitation is Lorentzian; for the 206-Å laser, it has a FWHM of 14 mÅ and for the 182-Å laser it has a FWHM of 9 mÅ.

Doppler broadening and collision broadening are correlated in principle through the velocity dependence of the collision cross section [69], but this correlation can be ignored for electron-ion collisions because of their great disparity in mass. The line profile including Doppler broadening and lifetime broadening due to spontaneous emission and inelastic electron-ion collisions is thus a Voigt profile; for the 206-Å laser, the Gaussian FWHM is 36 mÅ, the Lorentzian FWHM is 14 mÅ, and the total FWHM is 43 mÅ, while for the 182-Å laser the Gaussian FWHM is 32 mÅ, the Lorentzian FWHM is 9 mÅ, and the total FWHM is 37 mÅ.

Other broadening mechanisms, such as ion Stark broadening, elastic electron-ion collision broadening, and turbulence broadening, will certainly be present to some extent; however, we performed a calculation of the first two of these, which indicated that the net line profile due to quasistatic ion Stark broadening and elastic electron-ion collision broadening is approximately 2–3 mÅ wide for the 206-Å laser, so that these effects are small corrections only. This line profile calculation was based on the usual separation of the effects of fast electron impact collisions and quasistatic Stark effects due to slowly moving ions in the plasma. In this approximation, the Stark effect due to the ion microfield at the radiator splits each radiative transition into a number of components, and fast electron collisions then homogeneously broaden each of these components. Assuming that the ions are static during the radiation process, an average over the ion microfield perturbation at the radiator is performed; this results in an inhomogeneous broadening contribution to the line shape. The calculation used an atomic model based on a multiconfiguration Dirac-Fock atomic structure program [70]. The atomic structure for the $n=3$ level of Ne-like Se contains all *nlj* states and their cross couplings; perturbations of the $n=3$ to 3 transitions by levels beyond the $n=3$ principal quantum number were checked and found to be negligible for the conditions of interest.

The above discussion of Doppler broadening explicitly required the approximation that the moving radiators do not collide with one another. The breakdown of this approximation can lead to interesting effects and in particular can lead to a narrowing of the Doppler profile, as was first pointed out by Dicke [65]. This effect is examined in some detail here because it has been suggested that Dicke narrowing could be significant in Se x-ray lasers [31], though more recent and accurate calculations indicate that this may not be the case [43].

Collisional narrowing can be understood in terms of the correlation function Eq. (2) for a moving radiator. The nonoscillatory part of the Doppler-broadening time correlation function $g(\tau)$ Eq. (11) (neglecting collisions) was

$$g(\tau)=\exp\left[\frac{-k_0^2\tau^2\bar{v}^2}{4}\right], \quad \bar{v}=\left[\frac{2kT}{m}\right]^{1/2}, \tag{22}$$

so that the characteristic Doppler correlation time τ_0 is

$$\tau_0\approx\frac{1}{k_0\bar{v}}\approx\frac{\lambda_0}{\bar{v}} . \tag{23}$$

This is approximately the time taken for a radiator with a mean thermal velocity $\bar{v}$ to move a distance equal to the emission wavelength λ_0 (for Se this is $\tau_0\approx700$ fs). Since the spectral line profile is given by the Fourier transform of Eq. (22), it is clear that any effect which increases the effective decay time for the autocorrelation function Eq. (2) (by restricting radiator motion, e.g., through velocity-changing collisions) and does not itself degrade the phase correlation of the radiation will result in a narrower line profile [65,32]. This requirement implies that the velocity-changing collisions should not affect the internal state of the radiator, producing, for example, phase shifts in the emitted radiation which will introduce further spectral broadening [65,61]. The line is seen to narrow essentially because velocity-changing collisions effectively increase the mean time a radiator takes to move a straight-line distance equal to λ_0, so that Dicke narrowing can be considered to be a gas-phase analog to the solid-state Mössbauer effect in which recoil-less photon emission nullifies Doppler shifts and produces spectral narrowing [71]; however, it should be understood that Dicke narrowing is not a quantum-mechanical effect and can be derived for a classical oscillator moving classically (e.g., the original derivation in reference [65]).

The increase in correlation time due to collisions evidently can only occur when the mean collision interval τ_c is less than the Doppler correlation time τ_0, or

$$\tau_c<\tau_0=\frac{\lambda_0}{\bar{v}} . \tag{24}$$

The mean collision time is related to the mean free path λ_{ii} through

$$\tau_c=\frac{\lambda_{ii}}{\bar{v}} \tag{25}$$

so that the Dicke narrowing criterion can be stated as [65,32]

$$\lambda_{ii}<\lambda_0 . \tag{26}$$

Thus Dicke narrowing effects need to be considered when the radiator mean free path between velocity changing collisions is less than or equal to the emission wavelength. The resulting shape of the collisionally narrowed Doppler spectral profile generally consists of a narrow (Lorentzian) central spike superimposed on a broader (Gaussian) plateau [65,61]; in the limit $\tau_c\ll\tau_0$ (equivalently, $\lambda_{ii}<\lambda_0$), the width of the central Lorentzian peak is approximately $2\pi\lambda_{ii}/\lambda_0\ll1$ times the conventional Doppler width [32].

A number of authors have examined Dicke narrowing since Dicke's original paper. Galatry [72] used a weak (soft) collision model and neglected possible additional pressure broadening (due to radiation phase shifts caused by the same velocity-changing collision) to derive a Dicke narrowed line profile, while Gersten and Foley [61] used a strong collision model and treated collisions which affect radiator phase as well as change radiator velocity. In particular, they showed that when the typical phase shift η caused by the velocity-changing collisions is significant (η not much less than π), the line profile is essentially determined by that pressure broadening (in the absence of other, uncorrelated broadening mechanism), while when the internal radiator phase correlation is only weakly affected by the collisions ($\eta\ll\pi$), and assuming the magnitude of the phase shift in a particular collision is uncorrelated to the magnitude of the velocity change in the same collision, the resulting (Lorentzian near line center) line profile has a width approximately equal to the sum of the pressure broadened width and the Dicke narrowed Doppler width. Rautian and Sobel'man [32] used kinetic equations to derive more general line profiles without relying on weak or strong collision limits, and also discussed the effect of a correlation between the phase shift and the velocity change in a collision; this additional correlation was found to yield asymmetrical line profiles. Additional details, derivations and theoretical and experimental references on these interesting effects can be found in the works of Herbert [73] and McMahon [74].

It has been suggested that Dicke narrowing effects could be significant for extreme ultraviolet transitions in dense laser-produced plasmas [75] because the mean free path of an ion between 90° deflections in a plasma can be estimated to be as short as several angstroms for densities $>10^{20}$ cm^{-3} [75], and in particular it has been suggested that Dicke narrowing in conjunction with enhanced ion-ion pressure broadening could help explain the $J=0$–1 anomaly (discussed in Sec. I) in selenium x-ray lasers [31]. Griem estimated the ion-ion collisional mean free path in the Se x-ray laser plasma to be significantly less than the laser wavelengths, so that the Dicke narrowing condition $\lambda_{ii}\ll\lambda$ would be satisfied for the $\sim$200-Å laser lines, potentially resulting in a narrowing of the Doppler profile by a factor of 3 [31]. For the 206-Å laser, however, the radiator phase shifts induced by these same collisions (caused essentially by Stark shifts of the levels during the time of interaction [30]) would be significant (on the order of 0.5–1 rad [31]); the condition $\eta\ll\pi$ would therefore not be satisfied, so that the line profile would also be broadened by these phase shifts, as discussed above. The net effect would be a narrowing of the 206-Å Doppler profile coupled with increased pressure broadening (due to the radiator phase shifts), resulting in a nontrivial line profile which could actually be substantially similar in width to the line profile expected by ignoring these effects entirely. The relevance of these line-profile complications to the observed low gain on the 182-Å laser relies on a number of auxiliary conditions, including especially the absence of enhanced pressure broadening in the 182-Å laser, the prediction of significant turbulence in the Se plasma, and the existence of significant diffractive losses for the 182-Å laser.

However, recent molecular-dynamics simulations [43] suggest that Dicke narrowing effects may not in fact be expected to be significant for the Se x-ray laser. The authors point out several reasons for the discrepancy with previous estimates, the most important of which are the inclusion of ionic Debye screening effects and dense plasma effects in the simulations which serve to increase the effective ion-ion mean free path. The inclusion of these effects increases the mean free path estimated in Ref. [31] by a factor of 5, making the mean free path equal to or greater than the laser line wavelengths; the authors conclude that Dicke narrowing is therefore essentially insignificant for the Se laser. As previously noted ([28 and above), the 206-Å experimental data are inconclusive as to the presence or absence of Dicke narrowing effects because Dicke narrowing in the 206-Å laser could be masked by other broadening introduced by ion-ion interactions, and the observed lack of saturation rebroadening in that laser could in fact be taken as support for the Dicke narrowing hypothesis [28]. However, the 182-Å data presented here suggests that Dicke narrowing of the 182-Å laser is not in fact occurring and that the intrinsic linewidth of that laser is consistent with Voigt-profile estimates. Based on these results, together with the calculations of Ref. [43], we conclude that Dicke narrowing can be ignored in the Se x-ray laser, and we do not include Dicke narrowing effects in the present line-broadening and laser line transfer calculations.

VI. SELENIUM LASER LINE TRANSFER MODELING

The modeling performed for this research is based on the approach of Casperson and Yariv [34]. The model uses rate equations, solved in the time-independent steady-state limit, to obtain local atomic level population densities within the laser medium as a function of local laser intensity and radiator velocity assuming the intrinsic line profile of the laser is a Voigt profile, with the Doppler component assumed to be inhomogeneous; these population solutions are then combined with a one-dimensional, uni-directional radiative transfer differential equation, yielding a laser line transfer equation for the laser spectral intensity as a function of frequency and amplifier length which can be approximated in the completely inhomogeneous and completely homogeneous limits. This approach has been used previously to model ASE laser linewidth versus amplifier length data similar to that obtained in this research (see, for example, [35,38]). The primary approximations are the use of rate equations, rather than the more complicated density-matrix approach (see, for example, [62,63,76]), and the neglect of time dependence and bidirectional amplification in the laser transfer equation. The former approximation is justifiable when the radiator phase correlation function Eq. (2) for the laser transition decays rapidly in time compared to other rates such as the spontaneous emission rate between the levels involved, and is justified in the present case primarily by the broad Doppler width [42]. The later approximation is reasonable upon consideration of the time scales of the observed emission duration (≈ 200 ps) and the transit time across a saturated amplifier (also ≈ 200 ps for the longest targets observed), but is difficult to justify without comparative calculations which do not make this approximation; we therefore performed such a calculation [42] and found no significant differences in the results, as will be discussed later in this section. In this model we neglect power broadening and Rabi splitting effects on the line profiles [77,78] in saturated lasers and we assume equal spontaneous emission, stimulated emission, and absorption profiles; essentially, a single intrinsic line profile is assumed for absorption and emission which is fixed and independent of the local laser intensity. The neglect of power broadening is justified in the present circumstances primarily by the large Doppler width, so that the width of the total intrinsic line profile (calculated above to be 43 mÅ for the 206-Å laser) is more than an order of magnitude wider than the linewidth due to collisional mixing between the upper and lower laser levels alone (approximately 1.5 mÅ, from Fig. 12). The latter rate essentially determines the saturation intensity, defined in Eq. (43) below, so that the laser must be well saturated (effective gain-length product ≈ 20 [78]) before power-broadening of the local intrinsic line profile has a significant effect on the output spectrum; gain-length products of ~ 20 are barely achieved in the longest targets used in the present experiments.

The present model is based on a three-level collisional excitation model for the Se laser, where inversion is attained and maintained through collisional excitation of the upper laser level from the ground state and all other levels are ignored. This model is not quantitatively accurate for predicting laser parameters such as the gain, but is relatively simple and results in tractable equations, the general form of which are expected to be accurate. We briefly outline the derivation here in order to highlight the important features; more details can be found in Refs. [29,42,79].

The velocity-dependent rate equations for a three-level laser can be written as (see, for example, [35,63,67])

$$\frac{dN_1(v,t)}{dt} = -N_1(v,t)(\Gamma_{12}+\Gamma_{13}) + N_2(v,t)(\Gamma_{21}+A_{21}) + N_3(v,t)\Gamma_{31}\ , \tag{27}$$

$$\frac{dN_2(v,t)}{dt} = N_1(v,t)\Gamma_{12} - N_2(v,t)[\Gamma_{21}+\Gamma_{23}+A_{21}+R_{23}(v)] + N_3(v,t)[\Gamma_{32}+A_{32}+R_{32}(v)]\ , \tag{28}$$

$$\frac{dN_3(v,t)}{dt}=N_1(v,t)\Gamma_{13}+N_2(v,t)[\Gamma_{23}+R_{23}(v)]-N_3(v,t)[\Gamma_{31}+\Gamma_{32}+A_{32}+R_{32}(v)]\ , \quad (29)$$

where the R_{32} and R_{23} are the stimulated emission and absorption rates

$$R_{32}(v)=\frac{\lambda_0^3 A_{32}}{8\pi hc}\int_0^\infty \phi(\nu,v)I(\nu)d\nu\ , \quad (30)$$

$$R_{23}(v)=\frac{g_3}{g_2}R_{32}(v)\ , \quad (31)$$

and the area-normalized homogeneous (Lorentzian) intrinsic line profile due to spontaneous emission and inelastic collision broadening is

$$\phi(\nu,v)=\frac{2}{\pi\Delta\nu_L}\frac{1}{1+\frac{4[\nu-\nu_0(1+v/c)]^2}{(\Delta\nu_L)^2}}\ . \quad (32)$$

The central frequency is Doppler shifted here by the radiator velocity v. The populations $N_{1,2,3}(v)$ are the population densities of atoms in the ground state, the lower laser level, and the upper laser level, respectively (units $\text{cm}^{-4}\,\text{s}$), with axial velocities between v and $v+dv$, so that, e.g., the integral of $N_1(v)$ over velocity v is the total density of atoms in the ground state. λ_0 and ν_0 refer to the unshifted 3–2 transition (laser) wavelength and frequency, respectively, and g_2 and g_3 are degeneracy factors.

The other terms in these equations are the spontaneous emission and electron collisional excitation and deexcitation rates between the levels (A's and Γ's above; the spontaneous 3–1 transition is dipole forbidden in the Se laser, and rates to and from levels other than these three are neglected in order to maintain a closed system, with $N_1+N_2+N_3=N=\text{const}$) and the laser spectral intensity $I(\nu)$ in $\text{W}\,\text{cm}^{-2}\,\text{Hz}^{-1}$. It should be pointed out that these rate equations treat Doppler broadening inhomogeneously because there are no rates transferring population between velocity groups (collisional redistribution, discussed in [64,80,81]), so that each atom is assumed to have a particular velocity v which cannot change. The possible effects of collisional redistribution will be discussed in Sec. VII.

In steady state, the time derivatives are set equal to zero, yielding the results

$$N_2(v)=\frac{\left[\alpha+\frac{g_2}{g_3}\beta R_{32}(v)\right]Nf(v)}{1+\gamma R_{32}(v)}\ , \quad (33)$$

$$N_3(v)=\frac{[\chi+\beta R_{32}(v)]Nf(v)}{1+\gamma R_{32}(v)}\ . \quad (34)$$

N is the total lasant ion density and $f(v)$ is the velocity distribution function along the z axis, assumed to have the thermal equilibrium Maxwellian form

$$f(v)=\left[\frac{m}{2\pi kT}\right]^{1/2}\exp\left[-\frac{mv^2}{2kT}\right]\ , \quad (35)$$

and α, β, γ, and χ are complicated expressions involving the various spontaneous emission and collisional excitation and deexcitation rates.

The gain coefficient of the laser is simply the difference between the stimulated emission cross section (times the upper level density) and the absorption cross section (times the lower level density); in the present velocity-dependent case, the expression must be integrated over velocity to obtain the gain coefficient in cm^{-1}, so that

$$g(\nu)=\int\sigma_{32}(\nu,v)\left[N_3(v)-\frac{g_3}{g_2}N_2(v)\right]dv\ , \quad (36)$$

or in the present notation,

$$g(\nu)=\frac{\lambda_0^2 A_{32}}{8\pi}\left[\chi-\frac{g_3}{g_2}\alpha\right]N\int\frac{f(v)\phi(\nu,v)dv}{1+\gamma R_{32}(v)}\ . \quad (37)$$

This can be rewritten for convenience, yielding the following expression for the frequency-dependent gain coefficient for a Voigt-broadened laser:

$$g_{\text{Voigt}}(\nu)=\frac{g_0}{V(\nu_0)}\int_0^\infty\frac{S(u)\phi(\nu,u)du}{1+\frac{1}{I_{\text{sat}}}\int_0^\infty I(\nu')\phi(\nu',u)d\nu'}\ , \quad (38)$$

where $S(u)$ is the Doppler line profile

$$S(u)=\frac{1}{\Delta\nu_D}\left[\frac{4\ln 2}{\pi}\right]^{1/2}\exp\left[\frac{-4\ln 2(u-\nu_0)^2}{(\Delta\nu_D)^2}\right]\ , \quad (39)$$

$\phi(\nu,u)$ is the homogeneous Lorentzian profile

$$\phi(\nu,u)=\frac{2}{\pi\Delta\nu_L}\frac{1}{1+\frac{4(\nu-u)^2}{(\Delta\nu_L)^2}}\ , \quad (40)$$

$V(\nu_0)$ is the Voigt profile evaluated at line center

$$V(\nu_0)=\int_0^\infty S(u)\phi(\nu_0,u)du\ , \quad (41)$$

g_0 is the small-signal gain coefficient at line center

$$g_0=\frac{\lambda^2}{8\pi}A_{32}\left[\chi-\frac{g_3}{g_2}\alpha\right]NV(\nu_0)\ , \quad (42)$$

and I_{sat} is the saturation spectral intensity

$$I_{\text{sat}}=\frac{8\pi hc}{\gamma\lambda_0^3 A_{32}}\ . \quad (43)$$

Finally, the gain-coefficient equation (38) can be approximated in the completely homogeneous and completely inhomogeneous limits (where the inhomogeneous and homogeneous line widths $\Delta\nu_D$ and $\Delta\nu_L$, respectively, are negligibly small). This results in the homogeneous gain coefficient

$$g_{\text{hom}}(\nu)=\frac{g_0}{\phi(\nu_0,\nu_0)}\frac{\phi(\nu,\nu_0)}{1+\frac{1}{I_{\text{sat}}}\int_0^\infty I(\nu')\phi(\nu',\nu_0)d\nu'} \quad (44)$$

and the inhomogeneous gain coefficient

$$g_{\mathrm{inhom}}(\nu)=\frac{g_0}{S(\nu_0)}\frac{S(\nu)}{1+\dfrac{I(\nu)}{I_{\mathrm{sat}}}} \; . \tag{45}$$

Equation (28) for the frequency-dependent gain coefficient is expected to be quite general within the limitations of the approximations used, and in particular is not restricted to the three-level model used to guide the derivation.

The time-independent, unidirectional line transfer equation used is (see, for example, [63,67])

$$\frac{dI(\nu,z)}{dz}=g(\nu)I(\nu,z)+\varepsilon(\nu) \; , \tag{46}$$

where $g(\nu)$ is the gain coefficient and $\varepsilon(\nu)$ is the spontaneous emissivity source term. This equation gives the incremental change in the spectral intensity $I(\nu,z)$ of a laser field propagating in the positive z direction in a medium with frequency-dependent gain and emissivity which are constant along the z axis.

The spontaneous emissivity term $\varepsilon(\nu)$ on the right-hand side of Eq. (46) is the rate at which spontaneous energy is added to the laser beam, per unit volume at frequency ν into the relevant solid angle (determined by geometrical considerations; see, for example, [63]). In the present one-dimensional case, this term is approximately (see, for example [63,67])

$$h\nu_0 A_{32}\eta \int N_3(v)\phi(\nu,v)dv \; . \tag{47}$$

The integral is necessary because of the explicit radiator velocity dependence in $N_3(v)$ and $\phi(\nu,v)$. η is a simple solid angle factor, given approximately by the aspect ratio of the amplifier ($\pi r^2/4\pi L^2$, where r is the amplifier radius and L is the amplifier length) in the absence of refractive or diffractive effects; as this is essentially a very rough accounting of the spontaneous emission addition to the laser beam, η will be assumed here for simplicity to be constant. Equation (46) then becomes

$$\frac{dI(\nu,z)}{dz}\approx g(\nu,z)I(\nu,z)+h\nu_0 A_{32}\eta N \times\int_{-\infty}^{\infty}\frac{[\chi+\beta R_{32}(v)]f(v)\phi(\nu,v)dv}{1+\gamma R_{32}(v)} \; . \tag{48}$$

For the present purposes, the term involving β on the right-hand side can be dropped for convenience. This can be justified by considering both the small-signal and saturated regimes, using the analytical solutions to Eqs. (27)–(29) for β and χ and using the numerical values from Figs. 12 and 13. This approximation simply allows the upper laser level population [for the purposes of spontaneous additions to $I(\nu,z)$] to go to zero in the saturated regime rather than to a nonzero value [as $I(\nu,z)$ grows large, the upper and lower laser levels will become statistically populated].

Using Eq. (38), these simplifications allow the transfer equation for a Voigt broadened laser to be written as

$$\frac{dI(\nu,z)}{dz}=\frac{j_0}{V(\nu_0)}\left[1+\frac{g_0 I(\nu,z)}{j_0}\right] \times\int_0^{\infty}\frac{S(u)\phi(\nu,u)du}{1+\dfrac{1}{I_{\mathrm{sat}}}\displaystyle\int_0^{\infty}I(\nu')\phi(\nu',u)d\nu'} \; , \tag{49}$$

where the effective peak (line-center) spontaneous emissivity j_0 into the solid angle of interest is

$$j_0=h\nu_0 A_{32}\eta N\chi V(\nu_0) \tag{50}$$

and the other terms are defined above. This result is essentially Eq. (2) of Ref. [34], in the present notation and with the inclusion of spontaneous emission as in Eq. (5) of Ref. [34] or in Eq. (5) of Ref. [82]. In the completely homogeneous (lifetime broadening) limit, Eq. (49) becomes

$$\frac{dI(\nu,z)}{dz}=\frac{j_0}{\phi(\nu_0,\nu_0)}\left[1+\frac{g_0 I(\nu,z)}{j_0}\right] \times\frac{\phi(\nu,\nu_0)}{1+\dfrac{1}{I_{\mathrm{sat}}}\displaystyle\int_0^{\infty}I(\nu')\phi(\nu',\nu_0)d\nu'} \; . \tag{51}$$

This is essentially Eq. (21) of Ref. [34]. In the completely inhomogeneous (Doppler) limit, Eq. (49) simplifies to

$$\frac{dI(\nu,z)}{dz}=\frac{j_0}{S(\nu_0)}\left[1+\frac{g_0 I(\nu,z)}{j_0}\right]\frac{S(\nu)}{1+\dfrac{I(\nu,z)}{I_{\mathrm{sat}}}} \; . \tag{52}$$

This is essentially Eq. (32) of Ref. [34]. This inhomogeneous limiting-case equation can be solved analytically and results in

$$\left[1+\frac{g_0}{j_0}I(\nu,z)\right]\exp\left[\frac{I(\nu,z)}{I_{\mathrm{sat}}-\dfrac{j_0}{g_0}}\right] =\exp\left[\frac{g_0 S(\nu)z}{S(\nu_0)\left[1-\dfrac{j_0}{g_0 I_{\mathrm{sat}}}\right]}\right] \; . \tag{53}$$

We note that the bidirectional solution for inhomogeneous broadening, appropriate for saturated amplifiers with lifetimes long compared to the light transit time and including both positive and negative traveling waves, can also be derived analytically, and the result is an equation essentially identical to Eq. (53) except that I_{sat} is there replaced by $I_{\mathrm{sat}}/2$.

The approach of the present modeling will be to find solutions to the three laser line transfer equations (49), (51), and (53) for the following three line profile models: (i) an inhomogeneous Gaussian with a 36 mÅ FWHM, chosen to model Doppler broadening alone in the 206-Å laser; (ii) a Voigt profile with a 36-mÅ inhomogeneous Doppler component and a 14-mÅ homogeneous Lorentzian component, chosen to model the expected Voigt parameters of the 206-Å laser; and (iii) a homogeneous Lorentzian with a 50 mÅ FWHM, chosen for purposes of comparison. The primary objective of the models is predict the target-length scaling of the 206-Å laser spectral linewidth for the intrinsic line profiles assumed, given the amplifier-length scaling of the laser intensity, which has been measured previously [23] and was measured in the present experiments along with the spectral linewidths; the 206-Å laser, rather than the 182-Å laser, is modeled because the number of data points for that laser is greater and because the saturation behavior of that laser was observed (the 182-Å laser was not saturated in any of these experiments). As such, calculated parameters such as the gain coefficient, saturation intensity, and spontaneous emissivity will not be used, but will be found instead by fitting the calculated intensity curves to experimentally measured data. A correlation between a calculated intensity curve and the corresponding calculated spectral linewidth curve is assumed, and this correlation will be shown to hold (at least for homogeneous broadening) even when a time-dependent, bidirectional line transfer model is used.

The transfer equations (49), (51), and (53) were each solved numerically for spectrally integrated intensity $\int I(\nu,z)d\nu$ versus z, with parameters g_0, j_0, and I_{sat} chosen so that the resulting calculated spectrally integrated intensity versus target length curves were each consistent with the spectrally integrated data of Fig. 8. This was done iteratively and the fit was judged qualitatively; this approach is adequate and preferable in simplicity to other approaches such as optimizing the parameters individually for each model or numerically optimizing the curves using a nonlinear least-squares fitting method. The resulting values for g_0, j_0, and I_{sat} were 5.5 cm^{-1}, 1.5×10^{-9} $\text{W}\,\text{cm}^{-3}\,\text{Hz}^{-1}$, and 1.7×10^{-4} $\text{W}\,\text{cm}^{-2}\,\text{Hz}^{-1}$, respectively. These values are in reasonable (order of magnitude or better) agreement with simple estimates based on the three-level collisional excitation model (3.2 cm^{-1}, 9×10^{-9} $\text{W}\,\text{cm}^{-3}\,\text{Hz}^{-1}$, and 1.8×10^{-3} $\text{W}\,\text{cm}^{-2}\,\text{Hz}^{-1}$, respectively [42]). Figure 14 shows the resulting calculated curves for the three intrinsic line profile models used along with the data from Fig. 8. The curves are all in good agreement with the data within experimental uncertainties; the slight differences between the curves can be attributed to the different line profile models and the different degrees of saturation rebroadening.

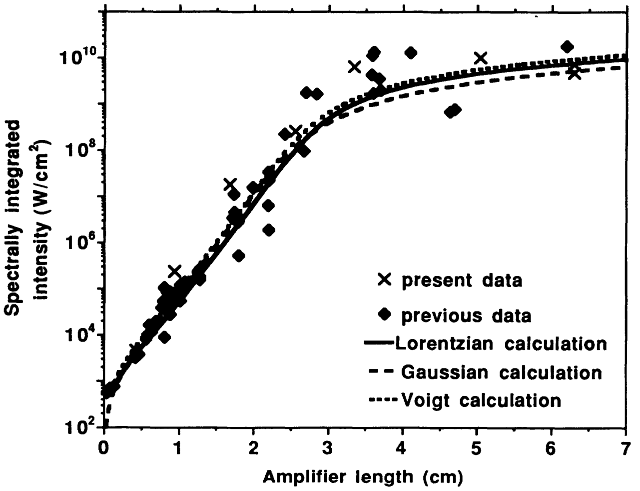

FIG. 14. Spectrally integrated intensity data (from Fig. 8) plotted with the calculated curves for the three intrinsic line profile models considered; a 50-mÅ homogeneous Lorentzian, a 36-mÅ inhomogeneous Gaussian, and a Voigt profile with a 36-mÅ inhomogeneous Gaussian component and a 14-mÅ homogeneous Lorentzian component.

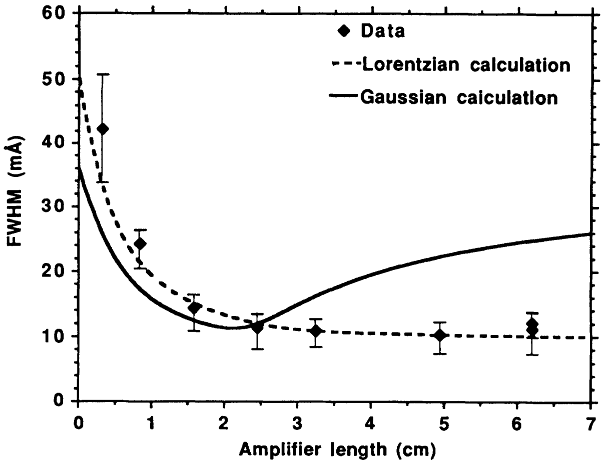

FIG. 15. Calculated laser linewidth versus amplifier length curves for the 50-mÅ homogeneous Lorentzian and 36-mÅ inhomogeneous Gaussian line profile models, plotted along with the experimental data from Fig. 10.

Figure 15 shows the corresponding calculated spectral

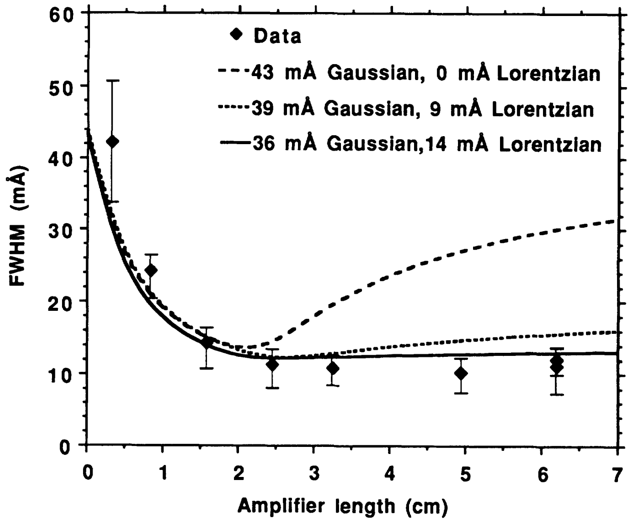

FIG. 16. Calculated laser linewidth versus amplifier length curves for three Voigt profiles, the first with a 36-mÅ inhomogeneous Gaussian component and a 14-mÅ homogeneous Lorentzian component (total 43 mÅ FWHM), the second with a 39-mÅ inhomogeneous Gaussian component and a 9-mÅ homogeneous Lorentzian component (total 43 mÅ FWHM), and the third with a 43-mÅ inhomogeneous Gaussian component alone (total 43 mÅ FWHM), plotted along with the experimental data from Fig. 10.

linewidth versus amplifier length curves for the 36-mÅ Gaussian and 50-mÅ Lorentzian intrinsic line profile models along with the experimental data, while Fig. 16 shows the calculated spectral linewidth versus amplifier length curve for the 36-mÅ Gaussian–14-mÅ Lorentzian Voigt-profile model. We discuss the results in the following section.

Finally, as discussed above, the present modeling approach fits the experimental intensity data to time-independent, unidirectional line transfer calculations in order to obtain the gain, saturation intensity, and spontaneous emissivity parameters. The primary assumption is that, given experimental data on the amplifier-length scaling of the laser intensity, the amplifier-length scaling of the laser spectral linewidth can be predicted for a particular intrinsic line profile model without reliance on calculated values for these parameters. A time-independent, unidirectional line transfer model is expected to be valid for reasons discussed above, but this expectation is difficult to test without comparison to a calculation which does not make these approximations. It therefore remains to be shown that the assumption of a correlation between the calculated intensity and the calculated spectral line width remains valid when time dependence in the gain, saturation intensity, and emissivity are accounted for in a bidirectional, time-dependent line transfer model.

An accounting of these effects with a Voigt intrinsic line profile model [29] would be difficult due to the complexity of the resulting equations, and such an attempt is beyond the scope of the research. However, these effects can be accounted for fairly simply with a homogeneous intrinsic line profile model. The relevant time-dependent, bidirectional transfer equations [equivalent to Eq. (51) above] are [35,63]

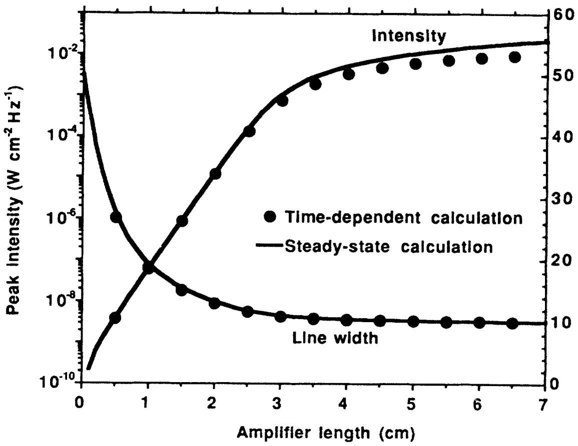

FIG. 17. Calculated peak spectral intensity and laser linewidth versus amplifier length curves for a 50-mÅ homogeneous Lorentzian line profile model using a time-dependent, bidirectional transfer model (points) and a time-independent, unidirectional transfer model (solid line).

$$\frac{1}{c}\frac{dI^{+}(\nu,z,t)}{dt}+\frac{dI^{+}(\nu,z,t)}{dz}=\frac{j_0(t)}{\phi(\nu_0,\nu_0)}\left[1+\frac{g_0(t)I^{+}(\nu,z,t)}{j_0(t)}\right]\times\frac{\phi(\nu,\nu_0)}{1+\frac{1}{I_{\mathrm{sat}}(t)}\int_0^\infty[I^{+}(\nu',z,t)+I^{-}(\nu',z,t)]\phi(\nu',\nu_0)d\nu'}\,, \tag{54}$$

$$\frac{1}{c}\frac{dI^{-}(\nu,z,t)}{dt}-\frac{dI^{-}(\nu,z,t)}{dz}=\frac{j_0(t)}{\phi(\nu_0,\nu_0)}\left[1+\frac{g_0(t)I^{-}(\nu,z,t)}{j_0(t)}\right]\times\frac{\phi(\nu,\nu_0)}{1+\frac{1}{I_{\mathrm{sat}}(t)}\int_0^\infty[I^{+}(\nu',z,t)+I^{-}(\nu',z,t)]\phi(\nu',\nu_0)d\nu'}\,. \tag{55}$$

We solved these equations numerically, using calculated curves for the time dependence of the gain, spontaneous emissivity, and saturation intensity from the XRASER model [83] which were normalized to the experimental intensity data as described above. These curves and the details of the calculations are discussed in Ref. [42]; we present here only the results. In Fig. 17 the results of the calculations using Eqs. (54) and (55) are compared directly to those using Eq. (51) above, assuming a 50-mÅ homogeneous Lorentzian intrinsic line profile. The intensity and spectral linewidth curves are essentially identical, implying that the neglect of time dependence and bidirectional amplification in the line transfer models is justified in the homogeneous line profile case and, likely, in the other cases as well.

VII. DISCUSSION AND CONCLUSIONS

It is clear from Fig. 15 that the 36-mÅ inhomogeneous Doppler line profile model is a poor approximation to experimental reality; the experimental intrinsic linewidth (extrapolated to $L=0$ in Fig. 15) is ~ 1.4 times broader than the predicted 36-mÅ Doppler width, and the saturation rebroadening predicted by inhomogeneous Doppler line transfer is not observed in the experiments. Arbitrarily increasing the Doppler linewidth to 50 mÅ improves the agreement in the small-signal regime, but worsens the agreement in the saturated regime [28]; we conclude that it is inaccurate to approximate the intrinsic line profile of the Se laser as being determined by inhomogeneous Doppler broadening.

The 50-mÅ homogeneous Lorentzian profile model yields a spectral linewidth vs amplifier length curve which does in fact agree with the experimental line width data (Fig. 15). The intrinsic linewidth of this model was chosen to agree with the experimental data, and the resulting line transfer calculation predicts a laser linewidth vs amplifier length curve which also agrees with the present experimental linewidth data. It is clear that this simple (and physically unrealistic) line profile model is quite adequate for calculating the Se laser linewidth as a function of amplifier length over the amplifier-length range investigated in the present experiments.

The 36-mÅ Gaussian–14-mÅ Lorentzian Voigt-profile model yields a linewidth vs amplifier length curve which is clearly a significant improvement over that found with the Doppler-alone model (Fig. 16). The intrinsic linewidth of this profile (≈ 43 mÅ FWHM) is somewhat less than the measured ~ 50 mÅ width, though it is possible that experimental uncertainties in this extrapolation (estimated to be ≈ 10 mÅ) are enough to include this value; the model also predicts slight but perhaps measurable saturation rebroadening in long targets. We conclude that this model (used, for example, in large simulation codes such XRASER [83]) is probably adequate for the purposes of predicting the laser linewidth for a given amplifier length to an accuracy of 10–20 %. Differences remain between the calculated results and the experimental data, but it is not clear that these differences are significant; more experimental data points would be required in order to make a conclusive comparison.

The lack of agreement between the present experimental Se laser linewidth data and the predictions of the Doppler-broadening model is interesting, as has been discussed previously [28,29,42]. The Se laser has generally been assumed to be dominated by Doppler broadening [1,2], Doppler broadening is generally an inhomogeneous broadening mechanism, and the calculated homogeneous lifetime broadening contribution is only one-third of the total linewidth; the lack of reasonable agreement between the experimental data and the Doppler-broadening calculation is therefore somewhat surprising. We conclude that the primary reason for the failure of this simple model to predict the saturation behavior of the laser is the very rapid decrease in saturation rebroadening obtained as the homogeneous contribution to the total linewidth is increased (Fig. 16); a 10-mÅ homogeneous linewidth significantly reduces the expected saturation rebroadening [28] and a 14-mÅ homogeneous linewidth nearly eliminates it.

As noted above, the Voigt-profile model appears adequate for most purposes, and the remaining differences between the calculated results and the experimental data may not be significant. We do, however, point out several features left out of the model which would improve the agreement with the experimental data. First, as discussed in Sec. V, additional broadening due to ionic electric fields and elastic electron-ion collisions is small but present, and these effects by themselves result in an intrinsic line profile with a 2–3 mÅ width. Additionally, turbulence in the plasma may be present [27,31]; this could be caused by bulk micrometer-scale turbulent motion in the plasma, resulting in a large number of local groups of atoms moving with different group velocities in addition to thermal velocities and resulting in additional line broadening with a width proportional to the average bulk flow velocity, on the order of the hydrodynamic flow velocities of $\sim 10^7$ cm/s [31,60]. The magnitude of such turbulent broadening is difficult to estimate given the large number of plasma physics processes which could cause such plasma nonuniformities [27], but it is quite possible that some additional broadening due to turbulence is present. These additional broadening mechanisms, neglected in the Voigt profile model, may account for at least part of the apparent remaining difference between the calculated Voigt intrinsic linewidth and the experimental extrapolation. We also note that the calculated Voigt width depends on the accuracy of the calculated electron collision rates and particularly on the calculated ion temperature; a slightly higher ion temperature (≈ 550 eV, rather than 400 eV) would increase the Doppler component of the intrinsic linewidth to 42 mÅ and increase the total Voigt width to 50 mÅ, in agreement with the estimated experimental extrapolation. Additional ion heating mechanisms not generally included in simulations but potentially significant are discussed in Ref. [84].

Finally, we note that any saturation rebroadening expected from the Doppler component may in fact be reduced or eliminated by collisional redistribution effects [64,80,81], as has been noted before [29,42]. The Doppler-broadening model developed in Sec. V explicitly ignored velocity-changing collisions, so that each ion was assumed to have an effectively constant velocity over time scales of interest (on the order of the radiative or electron-collisional lifetimes, the inverse of the lifetime-broadened linewidth ≈ 1 ps). If this approximation is not justified, then essentially different saturation behavior can be expected. In the limit where the velocity-changing collision frequency Γ_{ii} is much larger than the lifetime broadened linewidth $\Delta\nu_H$, the radiating and absorbing ions sample many velocities during their effective lifetimes, not just one. This collisional redistribution effect will essentially homogenize the Doppler component of the intrinsic line profile and would be expected to reduce the otherwise expected inhomogeneous saturation rebroadening [42]. It should be understood that these velocity-changing collisions are the same collisions which are responsible for Dicke narrowing in the limit $\Gamma_{ii} > \Delta\nu_D, \Delta\nu_D$ being the Doppler width. This limit is different from the collisional redistribution inequality $\Gamma_{ii} > \Delta\nu_H$ and the conditions are not as stringent simply because the expected Doppler width of 36 mÅ is significantly larger than the expected lifetime broadening width of 14 mÅ; there is therefore a regime where ion-ion collisions can affect the laser saturation behavior without significantly affecting the intrinsic line profile ($\Delta\nu_D > \Gamma_{ii} > \Delta\nu_H$). The ion-ion collision frequency from

Ref. [43] can be estimated as 1.5×10^{12} Hz (from a 400-eV ion temperature and a 200-Å mean free path), compared to the Doppler width of 2.5×10^{12} Hz (from 36 mÅ) and the lifetime broadened width of 9.9×10^{11} Hz (from 14 mÅ); it therefore appears that even though Dicke narrowing may not be significant in the Se laser, collisional redistribution effects may be. Inclusion of this effect in the line-transfer model developed above would be extremely difficult computationally [42], but it is clear from these estimates that collisional redistribution effects would need to be accounted for in accurate calculations of the saturation rebroadening expected from the Doppler component of the intrinsic line profile, and that any saturation rebroadening otherwise expected would likely be significantly reduced. This effect may help explain the unexpectedly reduced saturation rebroadening observed in other experiments with infrared lasers [38,79].

In summary, the main conclusions of this paper are the following. (i) The 206-Å laser data indicate an intrinsic linewidth for that laser of 50 mÅ, show gain narrowing of the line profile in the small-signal regime, and show no rebroadening of the line profile in the saturated regime. The extrapolated intrinsic linewidth is somewhat larger than the calculated Voigt width of 43 mÅ, but it is possible that the experimental uncertainties are large enough to include this value.

(ii) The 182-Å laser data indicate an intrinsic linewidth for that laser of 35 mÅ and show gain narrowing of the line profile in the small-signal regime; the saturated regime was not accessed for this laser. The extrapolated intrinsic width is consistent with the calculated Voigt width of 37 mÅ; this, together with recent calculations made in Ref. [43], suggests that Dicke narrowing effects are not significant.

(iii) Line transfer modeling shows that a Doppler-alone model for the intrinsic line profile of the 206-Å laser is inadequate, while a simple homogeneous Lorentzian model with a 50 mÅ width produces a laser linewidth vs amplifier length curve which agrees with the experimental data.

(iv) A Voigt-profile model for the intrinsic line profile of the 206-Å laser appears adequate for calculating the laser linewidth as a function of amplifier length to an accuracy of 10–20%. The apparent excess measured linewidth could be attributed to a combination of quasistatic ion Stark broadening and elastic electron collision broadening, turbulence broadening, and increased Doppler broadening due to higher ion temperatures; a 550-eV ion temperature, rather than 400 eV, would account for the excess linewidth entirely.

(v) Line transfer modeling indicates that saturation rebroadening of the 206-Å laser is significantly reduced by the homogeneous lifetime broadening component, even though this component is 30% of the Doppler width. In any case, collisional redistribution effects are likely to be present in the Se laser and would be expected to reduce or eliminate any saturation rebroadening from the Doppler component by effectively homogenizing the Doppler component.

We can suggest several avenues for relevant future research. First, existing ASE laser line transfer models we are aware of do not take collisional redistribution effects into account; it appears that this area needs further theoretical exploration, and we are aware of two recent papers which investigate this, including collisional redistribution effects with a relaxation model [79,85]. Second, existing ASE laser line transfer models which include power-broadening effects [77,78] treat Doppler broadening approximately, and a more complete model would account for power-broadening effects within the context of the present Voigt approximation to the intrinsic line profile; such a model would be computationally difficult, as has been noted before [78], but the effort might be justified if future x-ray laser experiments can demonstrate highly saturated output, particularly with injected-amplifier configurations. Finally, experimental linewidth data for Ni-like x-ray lasers has not been obtained and likely cannot be obtained with the instrument used for this research due to its poor short-wavelength efficiency; it is possible that other existing instruments might have sufficient resolution and efficiency to perform these experiments, at least for short amplifiers which do not produce significantly gain-narrowed output.

ACKNOWLEDGMENTS

We gratefully acknowledge assistance and support from K. Ackerman, C. Apuan, D. Attwood, T. Back, P. Bell, M. Campbell, J. Cardinal, M. Carter, C. Cerjan, K. Chapman, D. Clifford, D. Cochrell, J. Cox. M. Eckart, D. Fields, B. Flores, H. Griem, R. Haas, B. Hammel, P. Jautakis, R. Kauffman, J. Kilkenny, J. Kuhlman, O. Landen, S. Libby, N. Luhmann, D. McColm, E. Miller, J. Moreno, J. Nilsen, D. Nowak, A. Orel, M. Parish, B. Pasha, D. Phillion, J. Robinson, J. Scofield, G. Shimkaveg, B. Stewart, G. Stone, T. Thomson, J. Trebes, R. Walling, A. Wan, R. Wing, F. Wooten, G. Work, X. Zhu, and the staff at Nova, Tech Photo and the UCD Department of Applied Science. This work was performed under the auspices of the U.S. Department of Energy by the Lawrence Livermore National Laboratory under Contract No. W-7405-ENG-48 and by the Lawrence Berkeley Laboratory under Contract No. DE-AC03-76SF00098.

---

[1] D. L. Matthews, P. L. Hagelstein, M. D. Rosen, M. J. Eckart, N. M. Ceglio, A. U. Hazi, H. Medecki, B. J. MacGowan, J. E. Trebes, B. L. Whitten, E. M. Campbell, C. W. Hatcher, A. M. Hawryluk, R. L. Kauffman, L. D. Pleasance, G. Rambach, J. H. Scofield, G. Stone, and T. A. Weaver, Phys. Rev. Lett. **54**, 110 (1985).

[2] M. D. Rosen, P. L. Hagelstein, D. L. Matthews, E. M. Campbell, A. U. Hazi, B. L. Whitten, B. MacGowan, R. E. Turner, R. W. Lee, G. Charatis, Gar. E. Busch, C. L. Shepard, and P. D. Rockett, Phys. Rev. Lett. **54**, 106

(1985).

[3] S. Suckewer, C. H. Skinner, H. Milchberg, C. Keane, and D. Voorhees, Phys. Rev. Lett. **55**, 1753 (1985).

[4] R. C. Elton, *X-Ray Lasers* (Academic, San Diego, 1990).

[5] D. Desenne, L. Berthet, J.-L. Bourgade, J. Bruneau, A. Carillon, A. Decoster, A. Dulieu, H. Dumont, S. Jacquemot, P. Jaéglé, G. Jamelot, M. Louis-Jacquet, J.-P. Raucourt, C. Reverdin, J.-P. Thébault, and G. Thiell, *X-Ray Lasers 1990,* edited by G. J. Tallents (IOP, Bristol, England, 1991), p. 351.

[6] D. J. Fields, R. S. Walling, A. R. Fry, G. M. Shimkaveg, T. W. Phillips, A. L. Osterheld, B. J. MacGowan, L. B. Da Silva, R. E. Stewart, W. H. Goldstein, D. L. Matthews, and M. J. Eckart, *X-Ray Lasers 1990* (Ref. [5]), p. 131.

[7] D. J. Fields, R. S. Walling, G. M. Shimkaveg, B. J. MacGowan, L. B. Da Silva, J. H. Scofield, A. L. Osterheld, T. W. Phillips, M. D. Rosen, D. L. Matthews, W. H. Goldstein, and R. E. Stewart, Phys. Rev. A **46**, 1606 (1992).

[8] B. J. MacGowan, L. B. Da Silva, D. J. Fields, A. R. Fry, C. J. Keane, J. A. Koch, D. L. Matthews, S. Maxon, S. Mrowka, A. L. Osterheld, J. H. Scofield, and G. Shimkaveg, *X-Ray Lasers 1990* (Ref. [5]), p. 221.

[9] J. E. Trebes, S. B. Brown, E. M. Campbell, D. L. Matthews, D. G. Nilson, G. F. Stone, and D. A. Whelan, Science **238**, 517 (1987).

[10] B. J. MacGowan, S. Maxon, L. B. Da Silva, D. J. Fields, C. J. Keane, D. L. Matthews, A. L. Osterheld, J. H. Scofield, G. Shimkaveg, and G. F. Stone, Phys. Rev. Lett. **65**, 420 (1990).

[11] L. B. Da Silva, J. E. Trebes, S. Mrowka, T. W. Barbee, Jr., J. Brase, J. A. Koch, R. A. London, B. J. MacGowan, D. L. Matthews, D. Minyard, G. Stone, T. Yorkey, E. Anderson, D. T. Attwood, and D. Kern, Opt. Lett. **17**, 754 (1992).

[12] L. B. Da Silva, J. E. Trebes, R. Balhorn, S. Mrowka, E. Anderson, D. T. Attwood, T. W. Barbee, Jr., J. Brase, M. Corzett, J. Gray, J. A. Koch, C. Lee, D. Kern, R. A. London, B. J. MacGowan, D. L. Matthews, and G. Stone, Science **258**, 269 (1992).

[13] J. E. Trebes, K. A. Nugent, S. Mrowka, R. A. London, T. W. Barbee, M. R. Carter, J. A. Koch, B. J. MacGowan, D. L. Matthews, L. B. Da Silva, G. F. Stone, and M. D. Feit, Phys. Rev. Lett. **68**, 588 (1992).

[14] L. B. Da Silva, B. J. MacGowan, S. Mrowka, J. A. Koch, R. London, D. L. Matthews, and J. H. Underwood, Opt. Lett. **18**, 1174 (1993).

[15] N. M. Ceglio, D. G. Stearns, D. P. Gaines, A. M. Hawryluk, and J. E. Trebes, Opt. Lett. **13**, 108 (1988).

[16] A. Carillon, H. Z. Chen, P. Dhez, L. Dwivedi, J. Jacoby, P. Jaegle, G. Jamelot, Jie Zhang, M. H. Key, A. Kidd, A. Klisnick, R. Kodama, J. Krishnan, C. L. S. Lewis, D. Neely, P. Norreys, D. O'Neill, G. J. Pert, S. A. Ramsden, J. P. Raucourt, G. J. Tallents, and J. Uhomoibhi, Phys. Rev. Lett. **68**, 2917 (1992).

[17] J. H. Underwood and T. W. Barbee, Jr., Appl. Opt. **20**, 3027 (1981).

[18] Joseph Nilsen, Jeffrey A. Koch, James H. Scofield, Brian J. MacGowan, Juan C. Moreno, and Luiz B. Da Silva, Phys. Rev. Lett. **70**, 3713 (1993).

[19] J. E. Trebes, L. B. Da Silva, D. Ress, D. Lehr, R. A. London, S. Mrowka, and R. Procassini, Bull. Am. Phys. Soc. **38**, 2044 (1993).

[20] *Applications of X-Ray Lasers,* edited by R. London, D. Matthews, and S. Suckewer (The National Technical Information Service, Springfield, VA, 1992).

[21] C. J. Keane, SPIE Proc. **1551**, 2 (1991).

[22] Charles H. Skinner, Phys. Fluids B **3**, 2420 (1991).

[23] B. J. MacGowan, L. B. Da Silva, D. J. Fields, C. J. Keane, J. A. Koch, R. A. London, D. L. Matthews, S. Maxon, S. Mrowka, A. L. Osterheld, J. H. Scofield, G. Shimkaveg, J. E. Trebes, and R. S. Walling, Phys. Fluids B **4**, 2326 (1992).

[24] B. L. Whitten, M. H. Chen, A. U. Hazi, C. J. Keane, R. A. London, B. J. MacGowan, D. L. Matthews, T. W. Phillips, M. D. Rosen, J. E. Trebes, and D. A. Whelan, in *Proceedings of the International Conference on Lasers '88,* edited by R. C. Size and F. J. Duarte (STS, McLean, VA, 1989), p. 90.

[25] P. L. Hagelstein, Phys. Rev. A **34**, 924 (1986).

[26] B. J. MacGowan, L. B. Da Silva, D. J. Fields, C. J. Keane, S. Maxon, A. L. Osterheld, J. H. Scofield, and G. Shimkaveg, Phys. Rev. Lett. **65**, 2374 (1990).

[27] M. D. Rosen, Phys. Fluids B **2**, 1461 (1990).

[28] J. A. Koch, B. J. MacGowan, L. B. Da Silva, D. L. Matthews, J. H. Underwood, P. J. Batson, and S. Mrowka, Phys. Rev. Lett. **68**, 3291 (1992).

[29] J. A. Koch, B. J. MacGowan, L. B. Da Silva, D. L. Matthews, R. A. London, R. W. Lee, S. Mrowka, J. H. Underwood, and P. J. Batson, in *Spectral Line Shapes, Vol. 7,* edited by R. Stamm and B. Talin (Nova Science, Commack, NY, 1993), p. 205; Jeffrey A. Koch, Brian J. MacGowan, Luiz B. Da Silva, Dennis L. Matthews, Richard A. London, Richard W. Lee, Stan Mrowka, James H. Underwood, and Philip J. Batson, *Proceedings of the International Conference on Lasers '92* (STS, McLean, VA, 1993), p. 52.

[30] H. R. Griem, *Spectral Line Broadening by Plasmas* (Academic, New York, 1974).

[31] H. R. Griem, Phys. Rev. A **33**, 3580 (1986).

[32] S. G. Rautian and I. I. Sobel'man, Usp. Fiz. Nauk. **90**, 209 (1966) [Sov. Phys. Usp. **9**, 701 (1967)].

[33] A. Yariv and R. C. C. Leite, J. Appl. Phys. **34**, 3410 (1963).

[34] L. W. Casperson and A. Yariv, IEEE J. Quantum Electron. **QE-8**, 80 (1972).

[35] H. Maeda and A. Yariv, Phys. Lett. **43A**, 383 (1973).

[36] L. W. Casperson, J. Appl. Phys. **48**, 256 (1977).

[37] H. Gamo, J. S. Ostrom, and S. S. Chuang, J. Appl. Phys. **44**, 2750 (1973).

[38] D. H. Schwamb and S. R. Smith, Phys. Rev. A **21**, 896 (1980).

[39] J. A. Koch, L. B. Da Silva, B. J. MacGowan, D. L. Matthews, P. J. Batson, K. L. Chapman, and J. H. Underwood, in *Radiative Properties of Hot Dense Matter,* edited by W. Goldstein, C. Hooper, J. Gauthier, J. Seely, and R. Lee (World Scientific, Singapore, 1991), p. 373.

[40] J. A. Koch, P. J. Batons, M. R. Carter, K. L. Chapman, L. B. Da Silva, B. J. MacGowan, D. L. Matthews, S. Mrowka, J. H. Scofield, G. M. Shimkaveg, J. H. Underwood, and R. S. Walling, SPIE Proc. **1551**, 131 (1992).

[41] Y. Kato, H. Daido, H. Shiraga, M. Yamanaka, H. Azuma, K. Murai, E. Miura, G. Yuan, M. Ohmi, K. Tanaka, T. Kanabe, M. Takagi, S. S. Nakai, C. L. S. Lewis, D. M. O'Neill, D. Neely, K. Shinohara, M. Niibe, and Y. Fukuda, SPIE Proc. **1551**, 56 (1992).

[42] Jeffrey Allan Koch, Ph.D. thesis, University of California

at Davis, 1993 [available as Lawrence Livermore National Laboratory Report No. UCRL-LR-116938, 1993 (unpublished)].

[43] E. L. Pollack and R. A. London, Phys. Fluids B **5**, 4495 (1993).

[44] M. C. Hettrick, J. H. Underwood, P. J. Batson, and M. J. Eckart, Appl. Opt. **27**, 200 (1988).

[45] Additional details on these types of spectrometers are available in U.S. Patent Document 4,776,696, issued Oct. 11, 1988 to Michael C. Hettrick and James H. Underwood.

[46] Michael C. Hettrick and Stuart Bowyer, Appl. Opt. **22**, 3921 (1983).

[47] Michael C. Hettrick and James H. Underwood, in *Optical Science and Engineering Series 7,* AIP Conf. Proc. No. 147, edited by D. T. Attwood and J. Bokor (AIP, New York, 1986), p. 237.

[48] Joseph Nilsen and James H. Scofield, Phys. Scr. **49**, 588 (1994).

[49] D. S. Finley, S. Bowyer, F. Paresce, and R. F. Malina, Appl. Opt. **18**, 649 (1979).

[50] James Janesick and Tom Elliot, in *Astronomical CCD Observing and Reduction Techniques,* edited by S. B. Howell, Astronomical Society of the Pacific Conference Series No. 23 (Astronomical Society of the Pacific, San Francisco, CA, 1992), p. 1.

[51] P. Kirkpatrick and A. V. Baez, J. Opt. Soc. Am. **38**, 766 (1948).

[52] J. H. Underwood, Space Sci. Instrum. **3**, 259 (1977).

[53] J. H. Underwood and D. Turner, Proc. SPIE **106**, 125 (1977).

[54] See, for example, J. D. Kilkenny, Laser and Part. Beams **9**, 49 (1991), and references therein.

[55] B. J. MacGowan, J. A. Koch, and S. Mrowka, Rev. Sci. Instrum. **63**, 5122 (1992).

[56] See, for example, P. A. Jaanimagi and M. C. Richardson, Rev. Sci. Instrum. **54**, 1095 (1983), and references therein.

[57] Described in G. M. Shimkaveg, L. B. Da Silva, D. J. Fields, A. R. Fry, C. J. Keane, J. A. Koch, B. J. MacGowan, S. Mrowka, J. E. Trebes, R. E. Stewart, D. L. Matthews, and M. J. Eckart, *X-Ray Lasers 1990* (Ref. [5]), p. 105.

[58] M. D. Rosen, J. E. Trebes, B. J. MacGowan, P.L. Hagelstein, R. A. London, D. L. Matthews, D. G. Nilson, T. W. Phillips, D. A. Whelan, G. Charatis, G. E. Busch, and C. L. Shepard, Phys. Rev. Lett. **59**, 2283 (1987).

[59] D. A. Whelan, C. J. Keane, B. J. MacGowan, D. L. Matthews, J. E. Trebes, and M. J. Eckart, Proc. SPIE **831**, 275 (1987).

[60] J. C. Moreno, S. Goldsmith, and H. R. Griem, J. Opt. Soc. Am. B **9**, 339 (1992).

[61] Joel I. Gersten and Henry M. Foley, J. Opt. Soc. Am. **58**, 933 (1968).

[62] Bruce W. Shore, *The Theory of Coherent Atomic Excitation* (Wiley, New York, 1990), Vols. 1 and 2.

[63] Peter W. Milonni and Joseph H. Eberly, *Lasers* (Wiley, New York, 1988).

[64] P. W. Smith and T. Hänsch, Phys. Rev. Lett. **26**, 740 (1971).

[65] R. H. Dicke, Phys. Rev. **89**, 472 (1953).

[66] Mitchel Weissbluth, *Atoms and Molecules* (Academic, San Diego, 1978).

[67] George B. Rybicki and Alan P. Lightman, *Radiative Processes in Astrophysics* (Wiley, New York, 1979).

[68] Richard A. London, Mordecai D. Rosen, M. Stephen Maxon, David C. Eder, and Peter L. Hagelstein, J. Phys. B **22**, 3363 (1989).

[69] B. W. Fowler and C. C. Sung, J. Opt. Soc. Am. **65**, 949 (1975).

[70] I. P. Grant, B. J. McKenzie, P. H. Norrington, D. F. Mayers, and N. C. Pyper, Comput. Phys. Commun. **21**, 207 (1980).

[71] See, for example, Robert Eisberg and Robert Resnick, *Quantum Physics,* 2nd ed. (Wiley, New York, 1985).

[72] L. Galatry, Phys. Rev. **122**, 1218 (1961).

[73] Floyd Herbert, J. Quant. Spectosc. Radiat. Transfer **14**, 943 (1974).

[74] D. R. A. McMahon, Aust. J. Phys. **34**, 639 (1981).

[75] D. D. Burgess, D. Everett, and R. W. Lee, J. Phys. B **12**, L755 (1979).

[76] Murray Sargent III, Marlan O. Scully, and Willis E. Lamb, Jr., *Laser Physics* (Addison-Wesley, Reading, MA, 1974).

[77] Hans R. Griem, Phys. Rev. A **40**, 3706 (1989).

[78] Hans R. Griem and J. C. Moreno, Phys. Rev. A **44**, 4564 (1991).

[79] G. J. Pert, J. Opt. Soc. Am. B (to be published).

[80] Amado Y. Cabezas and Richard P. Treat, J. Appl. Phys. **37**, 3556 (1966).

[81] Anthony E. Siegman, *Lasers* (University Science Books, Mill Valley, CA, 1986).

[82] Gary J. Linford, Eugene R. Peressini, Walter R. Sooy, and Mary L. Spaeth, Appl. Opt. **13**, 379 (1974).

[83] P. L. Hagelstein, Plasma Phys. **25**, 1345 (1983).

[84] Richard M. More, *Atoms in Unusual Situations,* edited by J. P. Briand (Plenum, New York, 1966), p. 155.

[85] G. J. Pert (unpublished).

[86] J. A. Koch and B. J. MacGowan, J. Appl. Phys. **69**, 6935 (1991).

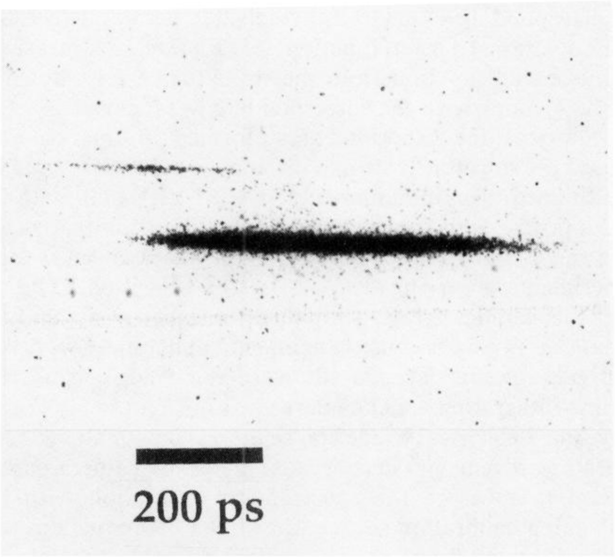

FIG. 6. 206.38-Å laser data from one of the 6.3-cm targets, obtained with an x-ray streak camera. Time is to the right and wavelength is down. The narrow streak at the upper left is a time fiducial (described in Ref. [86]).

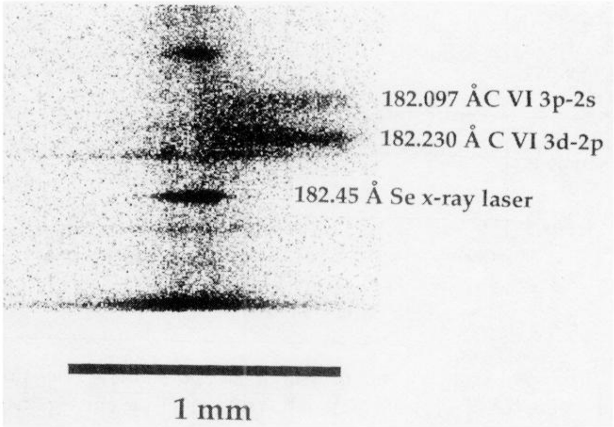

FIG. 7. 182.45-Å laser data from a 1.68-cm target, obtained with an x-ray CCD detector. Wavelength is down and space is to the right and left; the data are time integrated. The doublet above the Se laser is the H-like carbon Balmer α, originating from the Lexan side of the foil target; the other lines have not been identified. The contrast between the 3*d*-2*p* and 3*p*-2*s* peaks improves farther out in space because the densities are lower there, resulting in reduced Stark broadening.